Tofelde, S., Duesing, W., Schildgen, T., Wickert, A. D., Wittmann, H., Alonso, R. N., Strecker, M. (2018): Effects of deep-seated versus shallow hillslope processes on cosmogenic 10Be concentrations in fluvial sand and gravel. - *Earth Surface Processes and Landforms*, *43*, 15, pp. 3086—3098.

DOI: http://doi.org/10.1002/esp.4471

Effects of deep-seated versus shallow hillslope processes on cosmogenic ^{10}Be concentrations in fluvial sand and gravel

Stefanie Tofelde[*1,2], Walter Duesing[2], Taylor F. Schildgen[1,2], Andrew D. Wickert[3], Hella Wittmann[1], Ricardo N. Alonso[4,] Manfred Strecker[2]

[1]Helmholtz Zentrum Potsdam, GeoForschungsZentrum (GFZ) Potsdam, 14473 Potsdam, Germany.

[2]Institut für Erd- und Umweltwissenschaften, Universität Potsdam, 14476 Potsdam, Germany.

[3]Department of Earth Sciences and Saint Anthony Falls Laboratory, University of Minnesota, Minneapolis, MN 55455, USA.

[4]Departamento de Geología, Universidad Nacional de Salta, 4400 Salta, Argentina.

Abstract

Terrestrial cosmogenic nuclide (TCN) concentrations in fluvial sediment, from which denudation rates are commonly inferred, can be affected by hillslope processes. TCN concentrations in gravel and sand may differ if localized, deep-excavation processes (e.g. landslides, debris flows) affect the contributing catchment, whereas the TCN concentrations of sand and gravel tend to be more similar when diffusional processes like soil creep and sheetwash are dominant. To date, however, no study has systematically compared TCN concentrations in different detrital grain-size fractions with a detailed inventory of hillslope processes from the entire catchment. Here we compare concentrations of the TCN ^{10}Be in 20 detrital sand samples from the Quebrada del Toro (southern Central Andes, Argentina) to a hillslope-process inventory from each contributing catchment. Our comparison reveals a shift from low-slope gullying and scree production in slowly denuding, low-slope areas to steep-slope gullying and landsliding in fast-denuding, steep areas. To investigate whether the nature of hillslope processes (locally excavating or more uniformly denuding) may be reflected in a comparison of the 1^{0}Be concentrations of sand and gravel, we define the normalized sand-gravel index (*NSGI*) as the ^{10}Be-concentration difference between sand and gravel divided by their summed concentrations. We find a positive, linear relationship between the *NSGI* and median slope, such that our *NSGI* values broadly reflect the shift in hillslope processes from low-slope gullying and scree production to steep-slope gullying and landsliding. Higher *NSGI* values characterize regions affected by steep-slope gullying or landsliding. We relate the large scatter in the relationship, which is exhibited particularly in low-slope areas, to reduced hillslope-channel connectivity and associated transient sediment storage within those catchments. While high *NSGI* values in well-connected catchments are a reliable signal of deep-excavation processes, hillslope excavation processes may not be reliably recorded by *NSGI* values where sediment experiences transient storage.

Introduction

Terrestrial cosmogenic nuclides (TCN) have enabled the measurement of catchment-mean denudation rates over 10^2–10^6 year timescales (Bierman and Steig, 1996; Brown et al., 1995; Granger et al., 1996) and the tracking of changes in past denudation rates (e.g. Balco and Stone, 2005; Garcin et al., 2017; Schaller et al., 2004, 2002). However, it has been shown that the concentration of the TCN ^{10}Be ([^{10}Be]) in detrital sediment, from which catchment-mean denudation rates are commonly inferred, is affected by hillslope processes such as landslides (Puchol et al., 2014; West et al., 2014) and debris flows (Kober et al., 2012). In several cases, [^{10}Be] in detrital sediment has been shown to vary with grain size, which has been suggested to result from different hillslope processes mobilizing different grain-size distributions (Aguilar et al., 2014; Belmont et al., 2007; Carretier et al., 2015; Puchol et al., 2014; Schildgen et al., 2016). These observations imply that [^{10}Be] in fluvial sediments not only track denudation rates and their changes through time, but also preserve information about hillslope processes within the contributing catchment area. To date, however, there has been no systematic study comparing [^{10}Be] in different grain sizes to an inventory of hillslope processes within each contributing catchment.

Both TCN concentrations and grain-size distributions vary with depth. The *in-situ* production of ^{10}Be is greatest at the Earth's surface and decreases approximately exponentially with depth (**Fig. 1A**; Lal, 1991). At ~3 m depth, the production rate is close to zero. In addition, grain-size distributions tend to coarsen with depth (Puchol et al., 2014; Ruxton and Beery, 1957). While the abundance of sand tends to be higher close to the surface and decreases with depth, the abundance of gravel tends to increase with depth

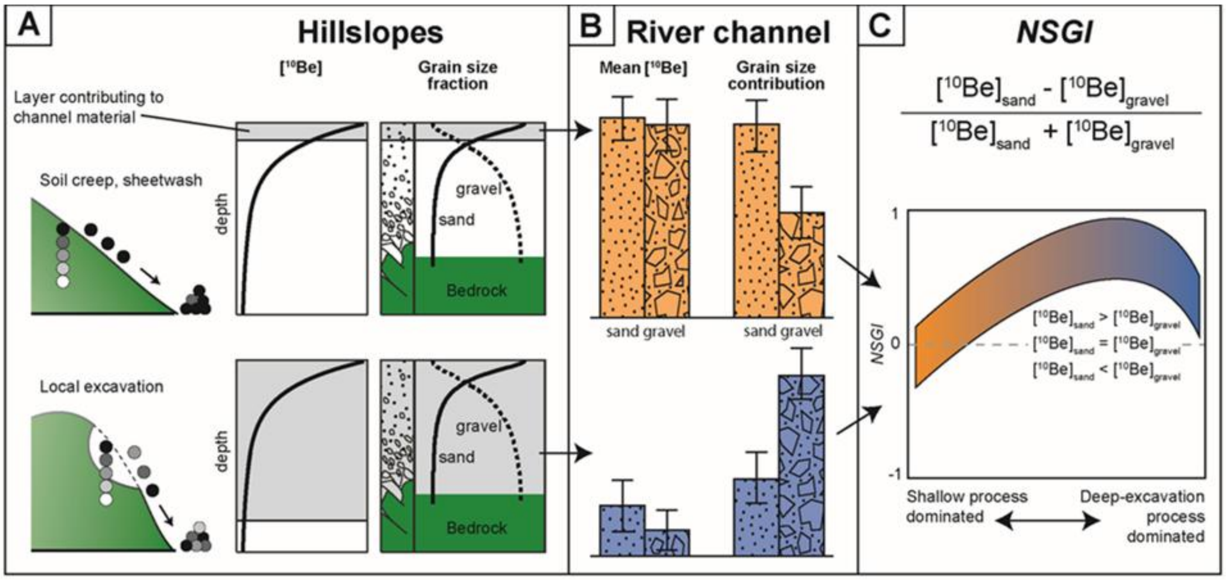

Figure 1 *Schematic diagram showing the derivation of the normalized sand-gravel index (NSGI) and hypothesized dependence on erosion processes. (A) ^{10}Be concentration ([^{10}Be]) of hillslope material decreases exponentially with depth (black to white circles and solid lines). The sand fraction is most abundant at the surface and decreases with depth, whereas gravel is more abundant in deeper layers less affected by weathering. (B) In soil creep or sheetwash dominated areas, the [^{10}Be] in detrital sand and gravel is higher than in areas influenced by local excavation processes, where the removal of deeper material results in the dilution of ^{10}Be in detrital sediments. Diffusional processes can mobilize more sand than gravel, whereas local excavation processes typically mobilize an increased amount of gravel. (C) For purely soil creep and sheetwash dominated areas, a NSGI of 0 ([^{10}Be]$_{sand}$ = [^{10}Be]$_{gravel}$) to -1 is expected. Negative values may result from slower hillslope transport of gravel compared to sand (e.g., Codilean et al., 2014). An increased abundance of local excavation processes should shift the NSGI toward more positive values. Highest NSGI values are expected when the majority of the gravel is contributed by deeper excavation events with low [^{10}Be]$_{gravel}$ and the majority of the sand contributed by shallow processes. The NSGI decreases again if deep-excavation events dominate the sampled sediment, and provide the majority of both the sand and gravel. The graphs of column A were modified from Puchol et al., (2014).*

due to less chemical weathering in deeper layers (Paasche et al., 2006; Puchol et al., 2014). In soil-mantled landscapes grain size distributions can deviate from this theoretical distribution due to the presence of a mixing layer (Riebe and Granger, 2013). If the surface is denuded uniformly and steadily throughout a catchment, the [^{10}Be] in fluvial sediment is inversely related to the mean denudation rate (Bierman and Steig, 1996; Brown et al., 1995; Granger et al., 1996; Lal, 1991). Deep-excavation processes such as landsliding can remove several meters of material instantly, and consequently contribute sediment with low [^{10}Be] to channels, resulting in higher catchment-mean denudation rates inferred from detrital sediment concentrations (Niemi et al., 2005; Puchol et al., 2014; West et al., 2014; Yanites et al., 2009). Landsliding or debris-flow activity also tends to produce coarser detrital material relative to processes like soil creep, because their mobilized material comprises a larger proportion of deeply-sourced, less-weathered, coarser material (**Fig. 1B;** Attal et al., 2015; Attal and Lavé, 2006; Roda-Boluda et al., 2018; Sklar et al., 2017). Consequently, [^{10}Be] in detrital gravel and sand fractions should be affected by hillslope erosion processes. We define the normalized sand-gravel index *(NSGI)* as the ^{10}Be concentration-difference between sand ([^{10}Be]$_{sand}$) and gravel ([^{10}Be]$_{gravel}$) normalized to their summed concentrations (**Fig. 1C**):

$$NSGI = \frac{[^{10}Be]_{sand} - [^{10}Be]_{gravel}}{[^{10}Be]_{sand} + [^{10}Be]_{gravel}} \qquad (1)$$

In areas dominated by diffusive hillslope processes like soil creep and sheetwash, fluvial sand and gravel is mainly sourced from near-surface layers with similar [^{10}Be], resulting in an *NSGI* of around 0 (**Fig. 1C**). If our assumptions about deep-excavation processes contributing coarser sediment with lower [^{10}Be] are correct, an increased contribution of those processes will lead to more positive *NSGI* values. The *NSGI* will peak near 1 when the majority of sand comes from diffusional processes with high [^{10}Be]$_{sand}$, while the majority of the gravel is contributed by deeper layers with low [^{10}Be]$_{gravel}$ that are mobilized by deep excavation processes. The *NSGI* should decrease again if deep-excavation events dominate the sampled sediment, and provide the majority of both the sand and gravel (e.g. landslide deposits). For such deposits, the *NSGI* would reflect the local [^{10}Be] difference of the sand and gravel fractions due to their sourcing from different depth layers (**Fig. 1A**). In areas characterized only by diffusive hillslope processes like soil creep and sheetwash, [^{10}Be]$_{sand}$ should be equal to or lower than [^{10}Be]$_{gravel}$ (*NSGI* = -1 to 0). Higher [^{10}Be] in gravel relative to sand, which would result in negative *NSGI* values, has rarely been reported, but has been attributed to the accumulation of ^{10}Be during slower transport of gravel compared to sand on gentle slopes (Codilean et al., 2014).

As a preliminary test of how different hillslope processes affect [^{10}Be] in different grain sizes, we first compare [^{10}Be] measured in fluvial sands collected from the Quebrada del Toro in the southern Central Andes to our mapped inventory of five distinct hillslope processes to investigate potential correlations among hillslope gradient, denudation rate, and hillslope processes. Second, we address whether a signal of hillslope processes is reflected in comparisons of [^{10}Be] in sand and gravel fractions, such that variations in erosion processes may be traced in sedimentary archives.

Study area

The Quebrada del Toro is a N-S oriented intermontane basin in the Eastern Cordillera of NW Argentina, which narrows southward where it traverses late Proterozoic basement rocks (**Fig. 2**). The basin is located between the arid Altiplano-Puna Plateau to the west and the humid foreland to the east, and it is bordered by reverse-fault bounded basement ranges. Activity on the Solá Fault in the west began in late Miocene time (Hilley and Strecker, 2005); to the northeast is the Gólgota Fault, which has been active since the Miocene and delimits the Sierra Pasha, a formerly glaciated range that forms an orographic barrier to precipitation (Marrett and Strecker, 2000). Exposed lithologic units in the ranges include late Proterozoic quartz-bearing metasediments, late Precambrian to early Cambrian granites, Cambrian quartzites, Cretaceous to Tertiary continental

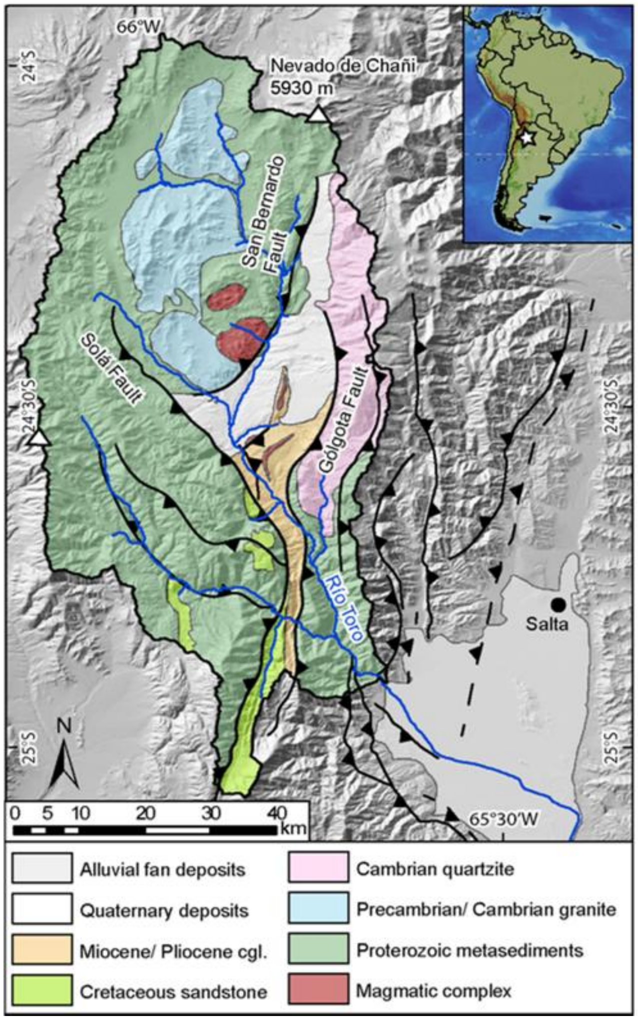

Figure 2 *Geological map of the Quebrada del Toro (modified after García et al., 2013; Hilley and Strecker, 2005; Tofelde et al., 2017). The intermontane basin is located within the Eastern Cordillera of the southern Central Andes (insert), with the Puna Plateau to its west and the foreland to its east. cgl. = conglomerate.*

sandstones, Cretaceous shallow marine limestones, Miocene to Pliocene conglomerates, and Quaternary gravels (Omarini et al., 1999; Reyes and Salfity, 1973; Schwab and Schäfer, 1976). The basin covers ~4000 km^2 between elevations of 1500 to 5900 m asl and is drained by the braided Río Toro. The region is subjected to ongoing deformation (García et al., 2013) and frequent, low-magnitude earthquakes (Hain et al., 2011).

Methods

Cosmogenic radionuclide analyses

We collected 15 detrital sand samples (250 – 500 µm) for ^{10}Be analysis along the Río Toro main stem (n = 4; sample prefix "M") and its tributaries (n = 11; sample prefix "T") to quantify denudation rates (**Table 1**). In 13 of those locations, we additionally sampled pebbles (1-3 cm, >65 clasts for each sample). The drainage areas of the main-stem samples range from 1495 to 2962 km^2, whereas the tributary catchments range from 9 to 779 km^2. Tributaries were sampled sufficiently far upstream to avoid admixing by main-stem material during flooding. In addition, we re-analyzed the ^{10}Be data from five previously published detrital sand samples from the Quebrada del Toro using an updated reference production rate (C1, C2, C3, C5, C6; Bookhagen and Strecker, 2012).

The sand and gravel samples were collected in March 2014. Mineral separation and quartz purification was carried out at the University of Potsdam, Germany. Sample preparation followed standard procedures (von Blanckenburg et al., 2004). First, samples were crushed (in the case of pebbles) and sieved. Next, quartz grains from the sand (250 – 500 µm) and crushed-pebble (250 - 1000 µm) samples were concentrated through magnetic separation. Subsequent chemical treatments with HCl and H_2O_2 dissolved carbonate and organic components. To dissolve non-quartz minerals and remove meteoric ^{10}Be, the samples were leached three times with a 1% HF/HNO_3 solution in an ultrasonic bath for 12 h each. Column chemistry and target preparation was performed at the GeoForschungsZentrum (GFZ) Potsdam, Germany, following standard procedures (i.e. von Blanckenburg et al., 2004). Prior to dissolution, 150 µg of a ^9Be carrier was added

***Table 1** Cosmogenic nuclide samples. CC= pebble samples, CS= sand samples, P(mu)= muon production rate, P(sp)= spallation production rate. Catchment-mean denudation rates calculated with a reference spallation production rate of 4.00 atoms/(g*yr) (Borchers et al., 2016) and the time-dependent scaling scheme of Lal (1991) and Stone (2000). All calculations were performed using the 07KNSTD ^{10}Be standard.*

Sample name	Latitude (°S)	Longitude (°W)	Drainage area (km^2)	Measured ^{10}Be / ^{9}Be	Error (%)	^{10}Be ± 1σ (atoms/g)	Topo. shield	P(mu) (atoms/g*yr)	P(sp) (atoms/g*yr)	Denudation rate ± 1σ (mm/yr)
M08_CC	24.54671	65.86952	2196	4.611e-12	3.07	939112 ± 28862				
M08_CS	24.54671	65.86952	2196	4.411e-12	3.06	869576 ± 26639	0.99	0.24	42.66	0.028 ± 0.0027
T11_CC	24.54951	65.86073	130	1.331e-12	3.16	247465 ± 7863				
T11_CS	24.54951	65.86073	130	8.935e-13	3.2	171990 ± 5559	0.99	0.22	36.81	0.112 ± 0.0105
M15_CC	24.49079	65.85755	1665	4.632e-12	3.06	916547 ± 28076				
M15_CS	24.49079	65.85755	1665	3.529e-12	3.08	691466 ± 21329	0.99	0.24	43.18	0.035 ± 0.0033
T26-CC	24.89980	65.67305	33	7.583e-15	15.06	1259 ± 1103				
T26-CS	24.89980	65.67305	33	1.329e-14	10.41	9547 ± 3383	0.95	0.18	23.13	1.232 ± 0.5100
T27-CC	24.84270	65.71425	9	7.286e-15	33.47	990 ± 1131				
T27-CS	24.84270	65.71425	9	1.873e-14	7.94	7457 ± 1697	0.96	0.16	19.17	1.337 ± 0.3398
T28-CC	24.64685	65.80950	114	3.048e-13	3.77	201980 ± 7977				
T28-CS	24.64685	65.80950	114	8.65e-13	3.38	189445 ± 6467	0.97	0.23	38.56	0.106 ± 0.0100
T32-CC	24.75050	65.74763	11	9.847e-14	4.96	27877 ± 1695				
T32-CS	24.75050	65.74763	11	2.525e-13	3.98	81981 ± 3462	0.95	0.20	28.49	0.181 ± 0.0174
T35-CC	24.36600	65.79750	100	2.119e-12	3.2	690382 ± 22155				
T35-CS	24.36600	65.79750	100	3.249e-12	3.13	445592 ± 13970	0.98	0.26	51.27	0.061 ± 0.0058
T43-CC	24.80866	65.80130	770	2.871e-14	8.41	7850 ± 1226				
T43-CS	24.80866	65.80130	770	4.288e-13	3.56	37265 ± 1365	0.97	0.23	42.01	0.541 ± 0.0513
T44-CC	24.81043	65.80020	176	7.568e-15	15.06	2169 ± 1906				
T44-CS	24.81043	65.80020	176	2.066e-13	4.04	18858 ± 826	0.96	0.23	40.40	1.033 ± 0.1009
M48_CS	24.79751	65.72750	2962	1.597e-12	3.13	322541 ± 10139	0.98	0.23	40.67	0.067 ± 0.0064
T59-CC	24.40490	65.82160	99	2.511e-12	3.16	768568 ± 24342				
T59-CS	24.40490	65.82160	99	1.349e-11	3.08	2173832 ± 66975	0.99	0.22	38.14	0.010 ± 0.0010
M60_CS	24.40700	65.81952	1495	4.673e-12	3.07	955189 ± 29355	0.99	0.24	44.15	0.026 ± 0.0025
T68_CC	24.49691	65.87763	474	4.856e-12	3.07	986599 ± 30319				
T68_CS	24.49691	65.87763	474	9.427e-12	3.05	1413630 ± 43136	0.98	0.23	42.39	0.017 ± 0.0017
T69_CC	24.56590	65.86406	79	4.562e-12	3.06	901168 ± 27606				
T69_CS	24.56590	65.86406	79	1.197e-12	3.17	943985 ± 30117	0.97	0.23	40.90	0.025 ± 0.0024
C1*	24.50169	65.86240	1672			745690 ± 14250	0.99	0.24	43.11	0.032 ± 0.0030
C2*	24.52355	65.87348	493			1510820 ± 18610	0.98	0.23	41.97	0.016 ± 0.0015
C3*	24.55461	65.86698	130			402260 ± 4590	0.99	0.22	36.77	0.050 ± 0.0045
C5*	24.72431	65.75522	178			314670 ± 5950	0.98	0.23	41.19	0.070 ± 0.0063
C6*	24.84070	65.72560	1011			38220 ± 1030	0.97	0.23	40.53	0.511 ± 0.0467
Blanks										
ST_Blk2**				3.061e-15	19.48					
ST_Blk3**				1.953e-15	23.14					
ST_Blk4**				9.654e-15	11.58					
ST_Blk1**				6.839e-15	15.91					
SS_Blk6**				6.898e-16	44.82					
BLK1				2.279e-15	25.19					
BLK2				1.678e-15	26.9					

ST_Blk6	6.701e-15	16.51
MDBLK1	8.26e-16	37.92
ST_Blk5**	5.113e-15	21.5
	3.879e-15	

* Samples previously published (Bookhagen and Strecker, 2012). ^{10}Be concentrations were extracted from the original publication, all further calculations were redone.

** Previously published blanks (Tofelde et al., 2017).

to each sample. Quartz was digested with concentrated HF (48%), and $Be(OH)_2$ was isolated via column chemistry. $Be(OH)_2$ was oxidized to BeO, mixed with Niobium, and prepared as targets for $^{10}Be/^{9}Be$ measurement with an accelerator mass spectrometer (AMS). AMS measurements were performed at the Department of Geology and Mineralogy, University of Cologne, Germany. The AMS standards used were KN01-6-2 and KN01-5-3; these have nominal $^{10}Be/^{9}Be$ ratios of $5.35*10^{-13}$ and $6.32*10^{-12}$, respectively. Blank corrections were performed using the average value of all 10 blanks processed during sample preparation (**Table 1**; a mean $^{10}Be/^{9}Be$ ratio of $3.88*10^{-15}$ was used for blank corrections of $^{10}Be/^{9}Be$ sample ratios).

The ^{10}Be concentration of fluvial sediment can be used to calculate catchment-mean denudation rates (ε) using the following equation (Lal, 1991):

$$\varepsilon = \left(\frac{P_0}{C_0} - \lambda\right)\frac{\Lambda}{\rho} \quad (2)$$

with P being the catchment-mean ^{10}Be production rate [atm/(g*yr)] and C the measured ^{10}Be concentration [atoms/g]; the subscript 0 on both refers to the surface (depth of zero). λ is the ^{10}Be decay rate [atoms/(g*yr)], Λ is the attenuation coefficient [g/cm^2] and ρ is the density of the eroding material [g/cm^3]. To solve this equation, we used the script of Scherler et al. (2014), which calculates the production rate first for each pixel within a catchment based on the reference production rate, the scaling scheme, and local shielding. Next, the script computes a catchment-mean production rate. For our analysis, we used a reference spallation-production rate of 4.00 atoms/(g*yr) (Borchers et al., 2016) and the time-dependent scaling scheme of Lal (1991) and Stone (2000), commonly known as the Lm-scaling scheme (Balco et al., 2008). In addition, we used the decay rate for ^{10}Be of 4.99 ± 0.043 10^{-7} yr^{-1} (Chmeleff et al., 2010; Korschinek et al., 2010), an attenuation coefficient of 160 g/cm^2, and a rock density of 2.7 g/cm^3. All calculations were performed using the 07KNSTD ^{10}Be standard. We report 1σ uncertainties for the denudation rates. The uncertainties are equivalent to the external uncertainties given by the CRONUS-Earth calculator (Balco et al., 2008) and include the analytical uncertainty of the ^{10}Be AMS measurement and the uncertainties of the reference spallation and muogenic production rates.

Hillslope-process inventory

We compared the ^{10}Be concentrations to a hillslope-process inventory that we created from Google Earth imagery, by mapping four non-diffusive, gravel-producing hillslope processes with a total of >8,500 polygons. We used the available historical imagery, with most images starting between 2003 and 2009. We named the four processes that we observed in the Quebrada del Toro *low-slope gullying, scree production, steep-slope gullying,* and *deep-seated landsliding* (**Fig. 3;** KML files containing our hillslope-process inventory can be found in the supplementary material). *Low-slope gullies* form rills in gently sloping sedimentary deposits (mostly Miocene to Quaternary in age) and mobilize gravel close to the surface. *Steep-slope* g*ullies* occur on steep slopes and are associated with debris-flows, which remove material from depths of

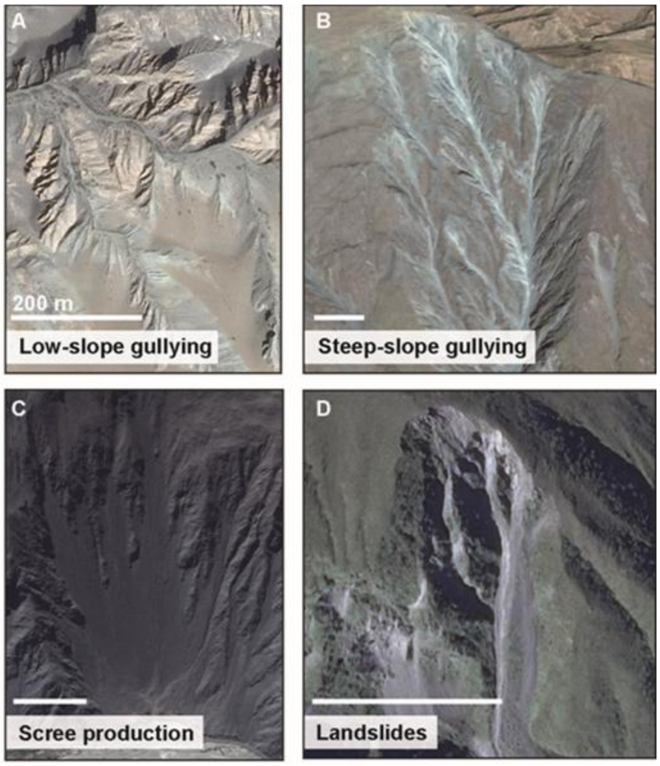

Figure 3 *The hillslope-process inventory is based on mapping in Google Earth. The four gravel-producing processes are (A) low-slope gullying (Image: Google, CNES/ Airbus, 2017), including the incision of first-order streams into Miocene to Quaternary sedimentary deposits; (B) gullying on steep slopes (Image: Google, CNES/ Airbus, DigitalGlobe, 2017), mostly associated with debris flows; (C) scree production (Image: Google, Google, CNES/ Airbus, 2017), mostly as a product of river undercutting followed by the formation of talus slopes, and (D) deep-seated landsliding (Image: Google, DigitalGlobe, 2017), characterized by stochastic events that instantly remove hillslope material up to several meters beneath the surface.*

up to several meters. *Scree production* occurs on steep slopes and is often related to river undercutting. *Deep-seated landslides* are rare, but tend to occur on steep slopes, where they mobilize rock from up to several meters depth. Moraine deposits visible in several locations above ~3700 m elevation indicate the former presence of glaciers. We mapped the extent of glaciers based on moraines and glacially carved valleys. However, the previously glaciated parts of the landscape today appear mainly diffusive, or are otherwise mapped as one of the areas characterized by the four non-diffusional processes. We summed the total area of each non-diffusive erosion process for each catchment using ArcGIS and defined the remaining area as characterized by diffusional processes, i.e., soil creep or sheetwash (**Table S1**). We make the assumption that the spatial distribution of those processes today is representative for the timescale over which the denudation rates average (10^2 to 10^5 yr).

Topographic analysis

Our stream network and slope analyses are based on the ~30-m-resolution SRTM digital elevation model (DEM) (data available from the U.S. Geological Survey). Slope is calculated for each pixel as the maximum rate of change in elevation between that pixel cell and its neighboring 8 cells. Based on that map, the slope distribution for each catchment and for the hillslope processes can be extracted. Then, a median slope value for the catchments and hillslope processes is calculated. We calculate the median rather than the mean slope due to the non-normal slope distributions, but the values differ by only 1 to 3 degrees for each catchment, and the choice of either does not affect the observed trends (**Table S2, Figure S1**). Previous studies have shown that the standard deviation of the slope depends on the resolution of the DEM (Ouimet et al., 2009). Instead of reporting the standard deviation, we additionally show the entire slope distribution from SRTM ~30-m data. Longitudinal river profiles were extracted in Matlab using the FLOWobj- and STREAMobj- functions provided by the TopoToolbox (Schwanghart and Scherler, 2014).

Results

Denudation rates and hillslope processes

Catchment-mean denudation rates derived from the sand samples range from 0.01 ± 0.001 to 1.34 ± 0.34 mm/yr (**Fig. 4A, Table 1**). Five additional denudation rates (C1,C2, C3, C5, C6) were recalculated from ^{10}Be data previously reported by Bookhagen and Strecker (2012). Three of those sites (C1, C2 and C3) were sampled near our sample locations; the associated denudation rates either agree within uncertainty (C1, C2) or within a factor of ~2 (C3) of our calculated rates. This difference is minor compared to the increase in denudation rates from N to S across the field area, which spans two orders of magnitude (**Fig. 4A insert**).

Catchment-mean denudation rates increase non-linearly with catchment-median slope (**Fig. 4B**). In detail, denudation rates increase linearly with median slope up to around 25°, beyond which they increase approximately exponentially. Denudation rates also increase non-linearly with normalized channel steepness index (k_{sn}) (e.g. Wobus et al., 2006) and relief, but those relationships show a weaker correlation **(Fig. S1, Table S2**).

Our hillslope-process inventory allows us to investigate how denudation rates and topographic metrics vary with hillslope processes. The pie charts (**Fig. 4B**) represent the proportional area covered by *low-slope gullying, steep-slope gullying, scree production,* and *deep-seated landsliding*. The numbers indicate the percentage of the catchment area covered by those four processes; the remaining area in each catchment is characterized by diffusional hillslope processes (soil creep or sheetwash). An asterisk indicates the

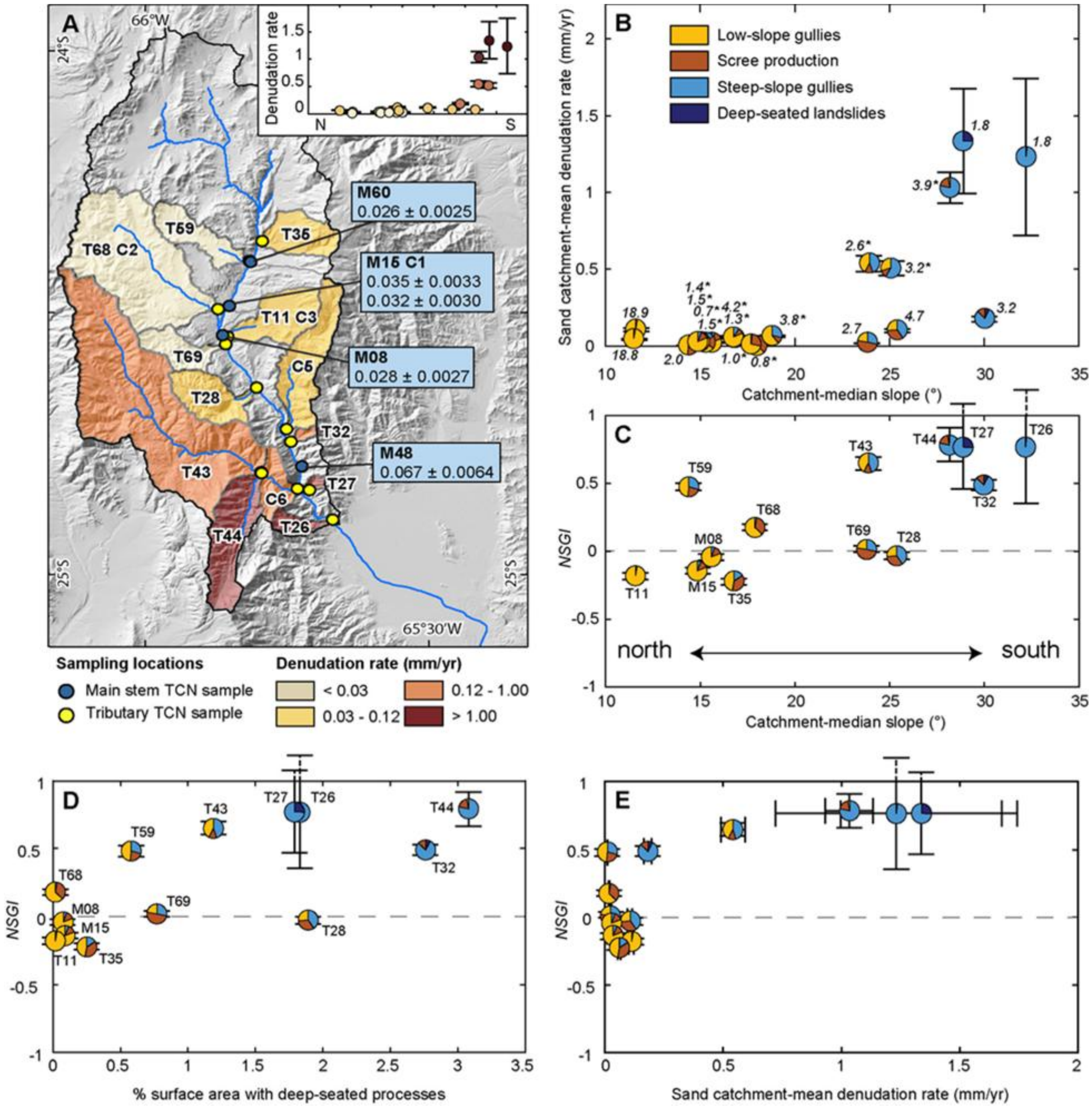

Figure 4 *(A) Sampling sites for detrital sand (n=20) and gravel (n=13, locations as indicated in C) along the main stem (blue, sample prefix "M") and tributaries (yellow, sample prefix "T"). Samples with the prefix "C" were recalculated from a previously published dataset* (Bookhagen and Strecker, 2012)*. The catchments are colored according to mean denudation rates, which were calculated from $[^{10}Be]$ in sand samples. The inset shows the increase in denudation rates by two orders of magnitude from N to S. (B) Catchment-mean denudation rates correlate non-linearly with catchment-median slope. Pie charts indicate the relative surface area influenced by low-slope gullying, scree production, steep-slope gullying, and deep-seated landsliding. The numbers depict the percentage catchment area affected by those four processes. Numbers with asterisks indicate the presence of moraines in the catchment. (C) The NSGI increases positively with catchment-median slope, and it increases overall with the occurrence of steep-slope gullying and landsliding. (D) The NSGI increases with percentage of catchment area affected by deep-seated processes, such as landslides or steep-slope gullying. (E) The NSGI shows a non-linear relationship with catchment-mean denudation rates derived from the sand fraction. Whereas slowly denuding areas experience some scatter in their NSGI, NSGI values become consistently larger than 0.5 and increase with higher denudation rates once catchment-mean denudation rates exceed ~0.2 mm/yr.*

presence of moraines in the catchment. Previously glaciated regions range from ~0.2 to ~15.7% of the catchment areas. We found no relationship between the formerly glaciated area and denudation rates, but we found a gradual shift in the type of erosion processes with increasing denudation rates and slopes. Apart from soil creep or sheetwash, low-gradient areas with low denudation rates are influenced by *low-slope gullying*. With increasing hillslope angles and denudation rates, *scree production* becomes more important, and when hillslope angles increase further, *steep-slope gullying* becomes more prevalent. Evidence for present-day *deep-seated landsliding* is sparse.

The total area covered by any of those four non-diffusive processes is small (0.7 to 18.8% of the catchment areas; **Table S1**). However, we only mapped areas with clear remnants of any of those four processes. The time for the visible recovery of the landscape after any localized mass-wasting event, however, is likely shorter than the recovery of the steady-state ^{10}Be depth profile in the bedrock. The mapped areal extents of non-diffusive processes are therefore likely underestimated with respect to the averaging timescale of the cosmogenic method.

Normalized sand-gravel index

We measured *NSGI* values between -0.22 and 0.79 (**Fig. 4C, Table S2**). The index values, although showing substantial scatter, increase linearly with catchment-median slope, indicating an increasing contribution of low $[^{10}\text{Be}]_{gravel}$ on steeper hillslopes. Negative *NSGI* values only occur in catchments characterized by low-gradient slopes, low denudation rates, and *low-slope gullying*, whereas positive values close to 1 occur in steep, rapidly eroding catchments influenced by *steep-slope gullying* and *deep-seated* *landsliding*. Furthermore, despite some scatter, we find that the *NSGI* increases with the proportion of the catchment surface area affected by *landslides* and *steep-slope gullies* (**Fig. 4D**). Overall, < 3.5 % of the total catchment areas are affected by these deep-seated process, but, we expect these numbers to be underestimated due to the restriction of the hillslope-process mapping to the last ~10 years of available imagery.

The non-linear increase of denudation rate with slope and the linear increase of *NSGI* with slope result in a non-linear relationship between denudation rate and *NSGI* (**Fig. 4E**). Slowly denuding areas reveal a range of *NSG*I values between -0.22 and 0.5. Once denudation rates exceed ~0.2 mm/yr, *NSGI* values exceed 0.5 and increase with higher denudation rates.

Discussion

Correlation between denudation rates and hillslope processes

The non-linear increase in ^{10}Be-derived catchment-mean denudation rates with catchment-median slope in our dataset (**Fig. 4B**) is in agreement with earlier studies (e.g. Binnie et al., 2007; Carretier et al., 2013; DiBiase et al., 2010; Ouimet et al., 2009; von Blanckenburg et al., 2004). As noted by those studies, whereas the mean or median hillslope gradient tracks catchment-mean denudation rates for lower slopes, this topographic metric becomes insensitive to changes in erosion rate in steeper areas, when hillslopes reach threshold angles. It has been suggested that once river incision creates hillslopes steep enough to initiate landsliding, any further increase in river down-cutting is accommodated by an increase in landslide frequency and not by further steepening of slopes (Burbank et al., 1996). Field studies have supported this idea, by showing that despite having similar mean hillslope angles, inventory-based landslide erosion rates are highly variable and correlate well with exhumation rates (Bennett et al., 2016; Larsen and Montgomery, 2012). Both modeling studies and empirical observations support the idea that landslide activity influences the [^{10}Be] in fluvial sediments by introducing low-concentration material to channels, resulting in higher inferred denudation rates (Niemi et al., 2005; Puchol et al., 2014; West et al., 2014; Yanites et al., 2009).

In our study area, recent *deep-seated landslides* are rarely observed, despite the non-linear increase in denudation rates in steeper areas. We find a gradual shift in hillslope processes with increasing hillslope angles from *low-slope gullying*, to *scree production*, and finally to *steep-slope gullying* and *landsliding* (**Fig. 4B***)*. In particular, we find *steep-slope gullying* to be the most common process characterizing threshold hillslopes, rather than deep-seated *landsliding*.

We assume that all mapped hillslope processes erode to a different average depth per event, have different recurrence intervals, and consequently affect the [^{10}Be] in fluvial sediment to a different degree. To quantify the impact of those individual hillslope processes on [^{10}Be] in mobilized sediment, we would not only need to know the average depth per event and average recurrence, but also the vertical distribution of grain sizes. Because the current knowledge on grain size-distributions associated with various hillslope processes is limited (Attal et al., 2015; Attal and Lavé, 2006; Marshall and Sklar, 2012; Sklar et al., 2017), we cannot yet quantify the contribution of the individual hillslope processes to our measured [^{10}Be], nor can we quantify the sediment flux associated with each process. However, our dataset suggests that the non-linearity in the relationship between ^{10}Be-derived denudation rates and slope is not only linked to changing landslide frequency, but also to a shift in the type of hillslope processes occurring within the catchments.

Normalized sand-gravel index

To our knowledge, 17 studies to date have performed ^{10}Be analyses of both detrital sand (< 2 mm) and gravel (>1 cm) (detailed list in **Table S3**). In most cases, those studies found significant differences between $[^{10}Be]_{sand}$ and $[^{10}Be]_{gravel}$. Carretier et al. (2015) and Aguilar et al. (2014) summarized different mechanisms that may explain the common occurrence of lower $[^{10}Be]_{gravel}$ compared to $[^{10}Be]_{sand}$ (*NSGI* > 0). These are: (1) a large contribution of glacial pebbles with low $[^{10}Be]$ due to shielding by ice (e.g. Wittmann et al., 2007); (2) lithological variations leading to gravel production mainly at lower elevations, where ^{10}Be production rates are lower (e.g. Palumbo et al., 2009); (3) an over-representation of gravels from low elevations, because high-elevation gravels are comminuted during transport (e.g. Belmont et al., 2007; Matmon et al., 2003) (4) deep-excavation events exhuming coarse material with low $[^{10}Be]$ (e.g. Belmont et al., 2007; Brown et al., 1995; Puchol et al., 2014); (5) coarse material being primarily derived from steep, faster eroding slopes (e.g. Carretier et al., 2015; Riebe et al., 2015); or (6) the alteration of $[^{10}Be]$ in sand and gravel due to temporary storage within the catchment (e.g. Schildgen et al., 2016). Conversely, $[^{10}Be]_{sand}$ can be lower than $[^{10}Be]_{gravel}$ (*NSGI* < 0) when gravels are transported more slowly than sand across low-gradient slopes (Codilean et al., 2014). In the following, we will discuss for each of those processes (i) how the different mechanisms affect $[^{10}Be]$, (ii) if those mechanisms apply to our study area and, (iii) if they can explain the positive trend of *NSGI* with catchment-median slope in our dataset (**Fig. 4C**).

Glacial debris can increase the *NSGI* value, if the glacial deposits contribute more gravel than sand and if those gravels have a lower [^{10}Be] than the hillslope material due to shielding by glacial ice (Wittmann et al., 2007). In our study area, glacial moraines are present (as indicated in **Fig. 4B**), but we found no systematic relationship between *NSGI* and previous glacial cover: the catchments with the highest *NSGI* values experienced no visible glacial overprint.

Lithological variability can explain positive *NSGI* values, if gravel is exclusively derived from a rock type that only occurs at low elevations in the catchment, where ^{10}Be production rates are lower. Lithological variations are present in our study area (**Fig. 2**), but cannot explain the observed systematic increase in *NSGI* from north to south. In several catchments, only one lithology crops out - Proterozoic metasediments (**Fig. S2**). Among those catchments, we measured both very high *NSGI* values close to 1 (T26, T27) and low *NSGI* values close to 0 (T69, T28) (**Fig. 4C**).

Comminution of gravels during transport would result in an over-representation of gravel from lower elevations, where ^{10}Be production rates are lower. This mechanism probably affected our samples, but likely only to a minor degree. Attal and Lavé (2009, 2006) experimentally measured mean abrasion rates between 0.15 and 0.4 %/km for Himalayan quartzites, quartzitic sandstones, and granites. The lengths of our sampled tributaries range from ~4 to ~75 km. These lengths would imply a maximum possible grain-size reduction of 30% through abrasion, but in most cases less than 10% for the farthest-transported gravel. In another study from the Tsangpo-Brahmaputra catchment,

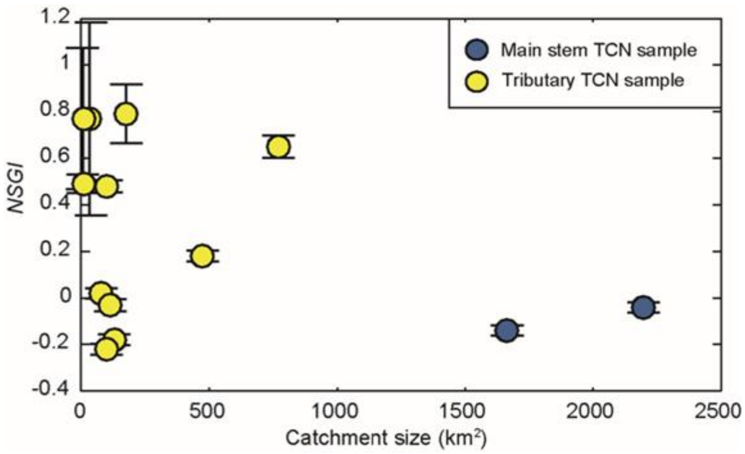

Figure 5 *Relationship between NSGI values and catchment size for tributary samples (yellow) and main-stem samples (blue); no correlation is observed. As such, attrition and upstream sediment storage, which are assumed to be more effective in larger catchments, cannot be the main drivers for the positive linear relationship between NSGI and catchment-median slope.*

Lupker et al. (2017) modelled abrasion to explain observed dilution in fluvial [^{10}Be]. They predicted that the effects of abrasion become apparent after 50 to 150 km, which is longer than the majority of our catchments. If the variations in *NSGI* in our study area were explained by an over-representation of gravels derived from low-elevations, we would expect a correlation between the *NSGI* and catchment size, but such a correlation does not occur in our dataset (**Fig. 5**).

The increase of *NSGI* values with median catchment slope in our dataset implies a higher contribution of low [^{10}Be]$_{gravel}$ in steep areas. Those steep areas are characterized by *steep-slope gullying* and *deep-seated landsliding* (**Fig. 4C**). As we assume that all hillslope processes contribute to the fluvial sand and gravel fractions, but that deep seated processes produce relatively more gravel and diffusional hillslope processes produce relatively more sand (**Fig. 1B**), two mechanisms can achieve lower [^{10}Be]$_{gravel}$ relative to [^{10}Be]$_{sand}$. One possibility is that the erosion depth and/or recurrence interval of deep-excavation processes increases with steeper slopes (Puchol et al., 2014), such that the

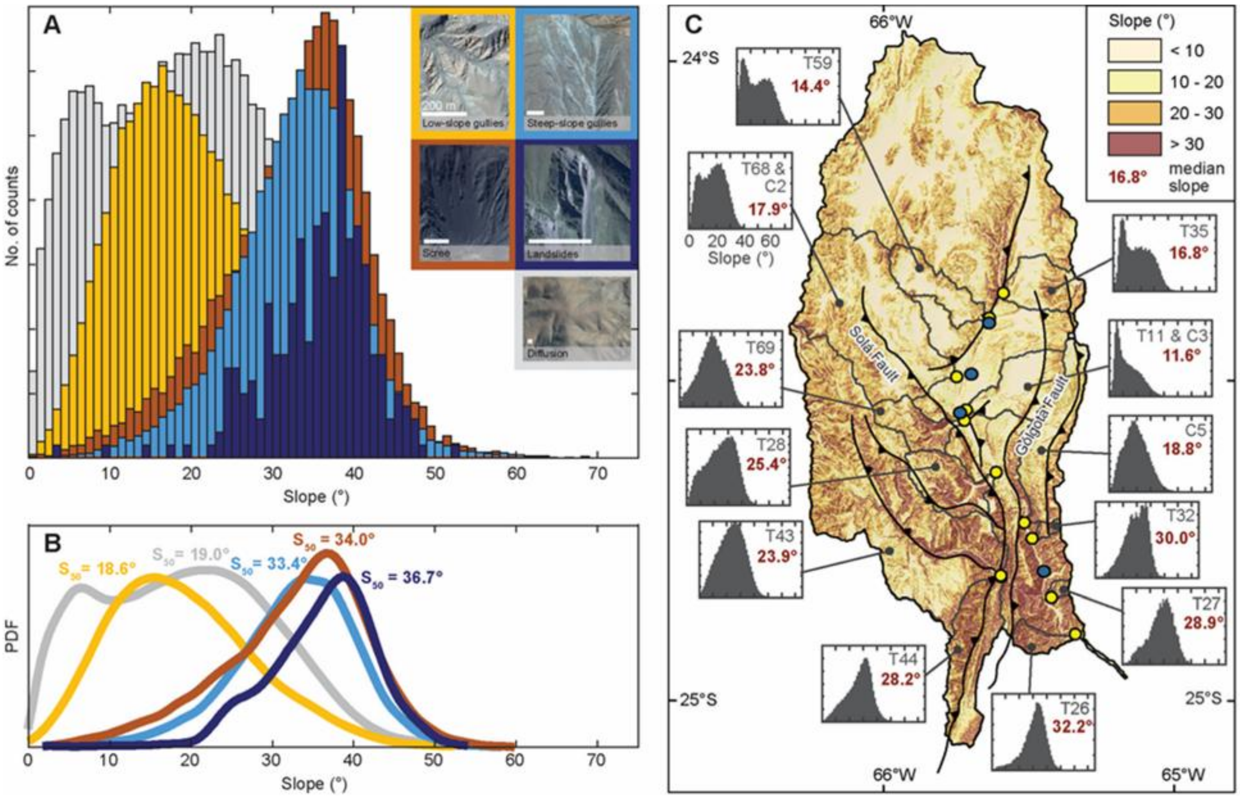

Figure 6 *Slope distributions of the five mapped hillslope processes represented as histograms (A) and best-fitted curves (B) together with the median slope for each process. Due to the great variability in abundance, the y-axes of (A) and (B) are scaled differently for each process for comparability. (C) Slope map of the Quebrada del Toro. Low-slope areas in the north are limited by the Solá and Gólgota faults. Insets show histograms of slope distributions for the sampled tributary catchments. Number indicates the median basin slope. Tributary slope distributions evolve from bimodal and with lower median slopes in the north to unimodal and higher median slopes in the south.*

$[^{10}Be]_{gravel}$ is diluted by deeply sourced gravel with low $[^{10}Be]$. Because deep-seated processes contribute relatively less sand, the $[^{10}Be]_{sand}$ is diluted less, and the difference between $[^{10}Be]_{gravel}$ and $[^{10}Be]_{sand}$ increases. Alternatively, the percentage of catchment surface area affected by deep-seated processes increases with steeper slopes (**Fig. 1C** moving to the right). Although we have no field measurements (e.g. landslide depths) to demonstrate the depths of the hillslope processes, it is probable that *landslides* erode to a greater depth per event than, for example, *scree production.* Previous studies have measured coarser sediment in landslides compared to non-landsliding hillslope processes, indicating greater erosional depths in landslides (Attal et al., 2015; Roda-Boluda et al., 2018; Whittaker et al., 2010). Thus, an increasing depth per erosion event and/or shorter recurrence intervals of excavation events with steeper slopes could help explain the linear increase of *NSGI* with catchment-median slope. We also observe an increase in *NSGI* with the proportion of the catchment surface-area affected by deep-seated processes (**Fig. 4D**). Hence, both mechanisms are likely to help explain the observed variations in *NSGI*.

If gravel-producing processes are not equally distributed throughout the catchment, but instead occur preferentially on steeper, faster eroding slopes, then the [^{10}Be] in gravel would be on average lower than in sand. The mapped non-diffusive hillslope processes in the Quebrada del Toro tend to occur on different hillslope angles (**Fig. 6A**). Whereas *low-slope gullying* mainly occurs on lower slopes (median slope 18.6°; **Fig. 6B**), the median hillslope angles increase for *steep-slope gullying* (33.4°), *scree production* (34.0°) *and deep-seated landsliding* (36.7°). The median slopes of *scree production*, *steep-slope gullying*, and *landsliding* are all higher than the median slope of the steepest catchment (T26: 32.2°). Thus, the processes that we infer to preferentially produce gravel tend to occur on steeper, faster eroding slopes within the catchments. The slope distributions of the catchments reveal a change from bimodal slope distributions in the north (e.g. T59, T68, T35) to unimodal distributions in the south with a shift towards a higher percentage of steeper slopes (e.g. T26, T27, T32, T44) (**Fig. 6C**). To explain higher *NSGI* values from the steeper catchments in the south, the gravel must be sourced primarily from deep-seated erosion processes occurring in areas of faster erosion, whereas the sand must be sourced more uniformly throughout the catchment (Aguilar et al., 2014; Carretier et al., 2015). This interpretation is supported by the fact that the change in slopes affects the [^{10}Be]$_{gravel}$ significantly more that [^{10}Be]$_{sand}$ (**Table 1, Fig. S3**).

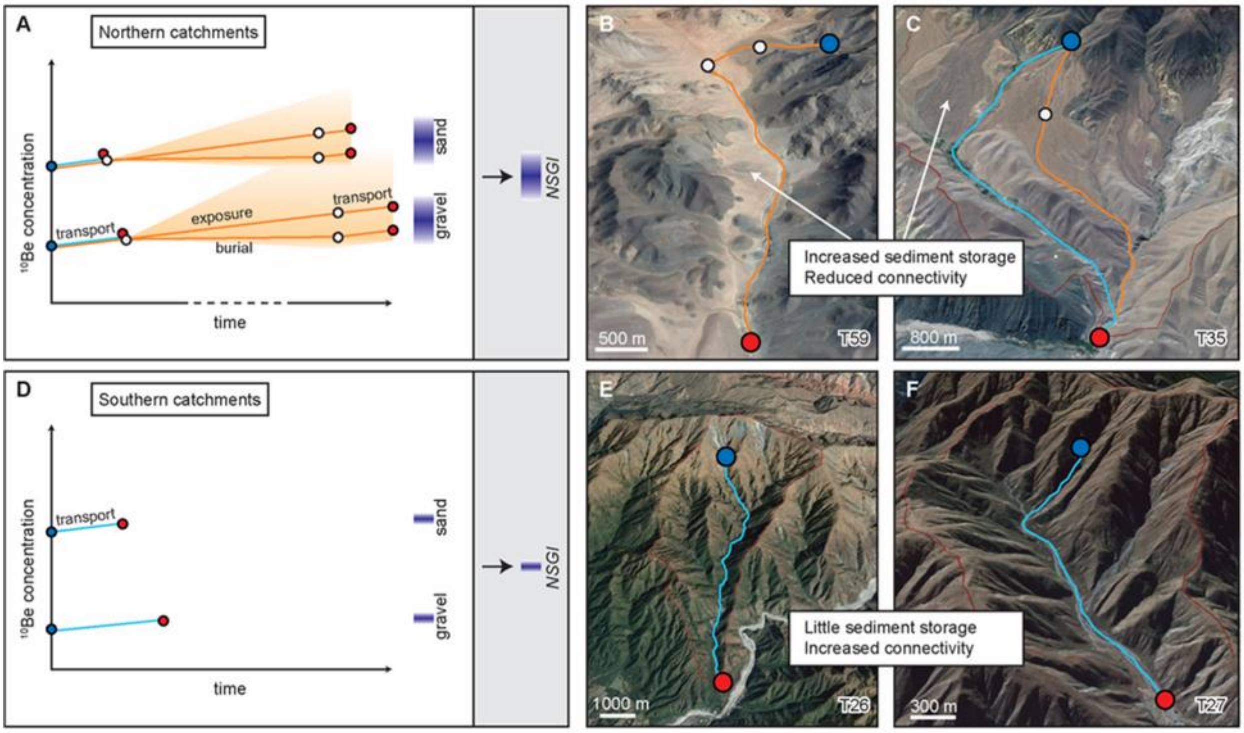

Figure 7 *(A) The evolution of [^{10}Be] in sand and gravel during transport and storage within the catchment. If gravel is derived, on average, from deeper in the profile, its [^{10}Be] is lower than that of the sand fraction. If those sediments are transported rapidly (blue line) from the hillslope (blue circle) to the catchment outlet (red circle), then additional accumulation of ^{10}Be during fluvial transport is low. The downstream transport of gravel is often slower compared to sand. However, if sediments are transiently stored in alluvial fans or fluvial terraces (white circle) and only later remobilized, the [^{10}Be] can significantly increase due to surface exposure, or slowly decrease when buried due to shielding from cosmic rays and subsequent nuclide decay. The sand grains or pebbles sampled at the outlet can consequently have diverse exposure and/or burial histories, which results in scatter of the NSGI. (B, C) Catchments in the north are characterized by significant sediment storage, which can reduce the hillslope-channel connectivity (Image A: Google, CNES/Airbus, 2018; Image B: Google, Digital Globe, CNES/Airbus, 2018). (D) Sand grains and pebbles collected at outlets experience a very similar transport history, such that [^{10}Be] signatures from the hillslopes remain largely unchanged and the NSGI values are consequently less scattered. (E, F) The catchments in the south show very little evidence for sediment storage, allowing for efficient downstream transport (Image D & E: Google, Digital Globe, CNES/Airbus, 2018).*

Upstream deposition of gravels and sand during transport can alter the [^{10}Be] in different ways. Transient sediment storage can result in prolonged sediment exposure and accumulation of ^{10}Be during slow transport, or it can result in a decrease in [^{10}Be] due to ^{10}Be decay during long-term burial (**Fig. 7A**). Consequently, in areas of low connectivity between hillslopes and river channels, the ^{10}Be signature of deep-excavation processes could be overprinted by inefficient sediment transport through the catchment. In contrast, low sediment storage space enables fast downstream transport of sediment with minimal effects on the [^{10}Be] in sand and gravel, and preservation of the original [^{10}Be] signatures in the sediment delivered from the hillslopes (**Fig. 7D**). In the field we observe a greater potential for sediment storage in the northern part of the study area, where Quaternary deposits in the form of alluvial fans and fluvial fill terraces are common (**Fig. 2, 7B & C**), while little sediment storage can be observed in the southern catchments (**Fig. 7E & F**). Topographic analysis confirms that the southern catchments, having relatively high *NSGI* values, show unimodal slope distributions with relatively high median slopes and concave-up river profiles, ensuring good connectivity between hillslopes and channels, which facilitates continuous transport of sediment downstream (**Fig. 6C, 8**). In contrast, the northern catchments, with relatively low *NSGI* values, are characterized by bimodal slope distributions, lower median slopes, and convex segments within their river profiles (especially T68 and T59) (**Fig. 6C, 8**). These convex segments are characterized by sedimentary fill in the form of Quaternary fluvial fill terraces (Tofelde et al., 2017), mass-failure of hillslopes (Marrett and Strecker, 2000; Mikuz, 2003), preserved lake sediments (Marrett and Strecker, 2000; Trauth and Strecker, 1999), and widespread alluvial-fan deposits (**Fig. 2, S2**). Overall, this evidence points to more transient sediment storage and a higher alteration potential of [^{10}Be] in the northern catchments. As such, upstream deposition of sediment does not explain the positive linear *NSGI*-slope trend, but is likely to explain why scatter in the relationship between *NSGI* and slope is larger in the northern catchments compared to the southern catchments (**Fig. 4C**).

Negative *NSGI* values were only measured in catchments with median slopes below 25° and are predominantly found in the northern, slowly denuding areas. We suggest that these negative values are a result of slower transport of gravel compared to sand on the gentle slopes, as has been noted in other low-slope regions (Codilean et al.,

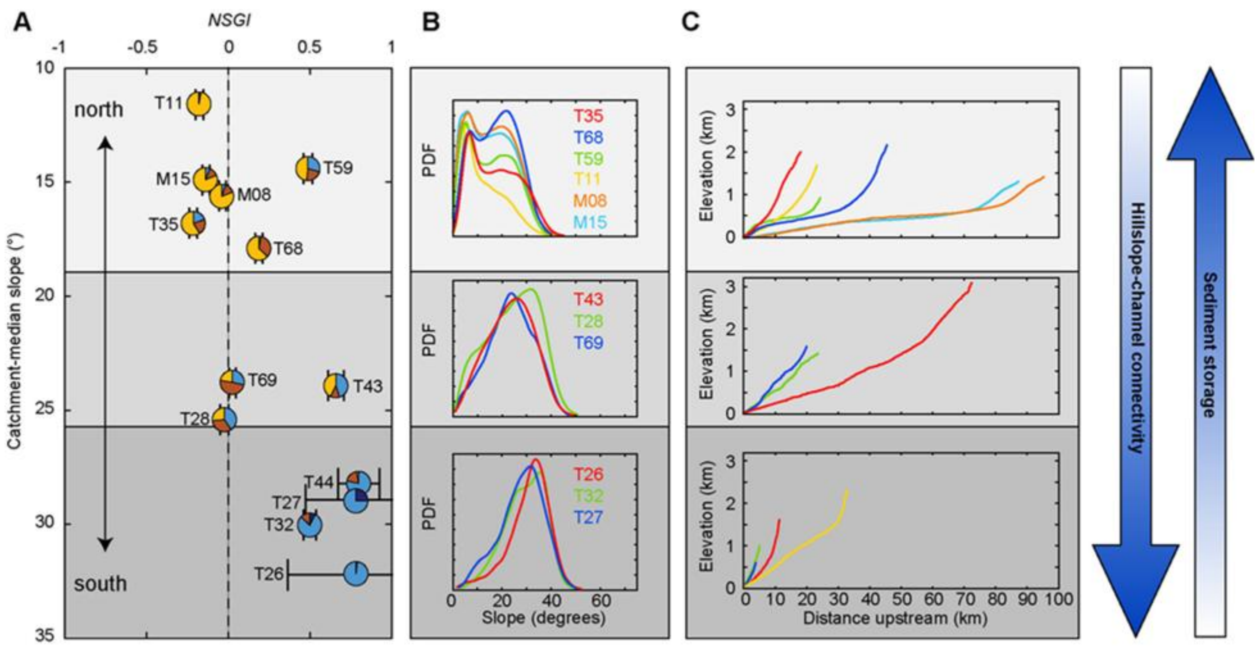

Figure 8 *(A) NSGI increases with catchment-median slope (same as Fig.4C). Separation of samples into three distinct domains based on their differences in NSGI, slope distributions, and river profiles (light grey to dark grey). (B) Best-fit slope distributions from all sample sites where sand and gravel were collected. The slope distributions evolve from a bimodal distribution with lower median slopes in the north to a unimodal distribution with higher median slopes in the south. (C) Longitudinal river profiles of the catchments. Elevations are relative to the sampling location. Profile shapes evolve from gentle, partly convex profiles in the north to steeper, concave-up profiles in the south. We interpret the channel geometries as an increase in hillslope-channel connectivity and increased uplift rates from north to south, while sediment storage within the catchments increases from south to north.*

2014). If transient sand and gravel are equally distributed with depth in the temporary sedimentary deposits, such that they are exposed to similar ^{10}Be production rates during downstream transport, then negative *NSGI* values could potentially be used to infer relative differences in sand and gravel residence times.

We infer that several previously described mechanisms that can alter [^{10}Be] in sand and gravel could have affected our samples. Only three of those mechanisms, however – (1) increasing depth and/or shorter recurrence intervals together with a rising percentage of surface area covered by deep-excavation events with increasing slopes, (2) gravel being primarily produced on steeper, faster eroding slopes, and (3) slow transport of gravel on gentle slopes – can explain the linear increase of *NSGI* with catchment-median slope. We suggest that transient sediment storage and the consequent alteration of [^{10}Be] in sand and gravel, particularly in the northern part of the basin, explain the majority of the observed scatter of the *NSGI*-slope relationship. We do not find clear evidence that glacial pebbles, lithological variation, or comminution affect the *NSGI*. However, we cannot rule out their contribution to the scatter in the *NSGI*-slope relationship.

In summary, in the Quebrada del Toro, the effects of deep-excavation processes in the southern catchments are captured well by high *NSGI* values. Lower *NSGI* values in the north partly reflect less prevalent deep-excavation processes (based on our hillslope-process inventory), but those samples are likely to have been affected by transient sediment storage and overprinting of the ^{10}Be signal in fluvial sand and gravel.

Catchment-mean denudation rates inferred from [^{10}Be] are typically measured in the sand fraction (e.g. Bookhagen and Strecker, 2012; Granger et al., 1996; Ouimet et al., 2009; Scherler et al., 2014; Wittmann et al., 2007), which is commonly assumed to be uniformly sourced throughout the catchment (Aguilar et al., 2014; Carretier et al., 2015). The non-linear relationship between *NSGI* and catchment-mean denudation rates reveals that the highest *NSGI* values coincide with the highest denudation rates (**Fig. 4E**). As originally hypothesized, most of these fast denuding catchments (T26, T27, T44 and T43) with high *NSGI* are characterized by a higher abundance of deep-seated processes (**Fig. 4D**), which not only contribute large amounts of gravel with low [^{10}Be], but also sand with low [^{10}Be]. Consequently, the calculated denudation rates for those catchments based on [^{10}Be]$_{sand}$ may be overestimated (e.g. Niemi et al., 2005; Yanites et al., 2009). In such cases, the *NSGI* could potentially be used not only as a tracer of hillslope processes, but also as a tool to detect biases in ^{10}Be derived denudation rates.

Conclusions

By combining [^{10}Be] measurements in sand and gravel with a detailed hillslope-process inventory, we demonstrate empirically a shift in hillslope erosion processes with increasing catchment-median slopes and ^{10}Be derived catchment-mean denudation rates. Specifically, rapid increases in denudation rates as hillslopes approach threshold angles are associated with increasing importance of *steep-slope gullying*, with a minor contribution from *landsliding*. As such, we suggest that the non-linearity in the cosmogenic nuclide-derived correlations between denudation-rate and slope are not only linked to the adjustment of landslide frequency, but also to a shift in the type of hillslope processes.

We find that the normalized sand-gravel index (*NSGI*) shows a linear, albeit scattered, increase with catchment-median slope, indicating an increased contribution of low [^{10}Be] gravel in steeper areas. By excluding other options, we conclude that the increase can only be explained if (i) non-diffusive hillslope processes contribute more gravel compared to sand, (ii) the erosion depth per event, the event frequency, and/or the affected surface area increases with higher slopes, and (iii) gravel is primarily produced on steeper, faster eroding slopes. The shift to higher *NSGI* values coincides with a shift in hillslope processes from *low-slope gullying* to *scree production* to *steep-slope gullying* and *landsliding*. As such, the *NSGI* may track changes in hillslope processes. However, the *NSGI*-slope correlation exhibits significant scatter. We explain the majority of the scatter, especially in lower-slope areas, by the limited hillslope-channel connectivity, which can delay the delivery of sediment with low [^{10}Be] to channels, providing more time for ^{10}Be accumulation or decay. While high *NSGI* values in the southern catchments appear to be a reliable signal of deep-excavation processes, lower *NSGI*-values in the northern catchments are a less reliable proxy for hillslope processes due to transient sediment storage and the potential for overprinting of [^{10}Be] in the sediment.

Acknowledgements

J. Schüürmann, L. Pollozek, D. Käter, M. Lang, and C. Schulz are thanked for help with sample processing and S. Binnie and S. Heinze for performing the AMS measurements. In addition, we would like to thank Sébastien Carretier and Maarten Lupker for highly constructive review comments. This study was funded by the Emmy-Noether-Programme of the Deutsche Forschungsgemeinschaft (DFG) grant number SCHI 1241/1-1 awarded to T.S.

References

Aguilar, G., Carretier, S., Regard, V., Vassallo, R., Riquelme, R., Martinod, J., 2014. Grain size-dependent 10Be concentrations in alluvial stream sediment of the Huasco Valley, a semi-arid Andes region. Quat. Geochronol. 19, 163–172. doi:10.1016/j.quageo.2013.01.011

Attal, M., Lavé, J., 2009. Pebble abrasion during fluvial transport: Experimental results and implications for the evolution of the sediment load along rivers. J. Geophys. Res. Earth Surf. 114. doi:10.1029/2009JF001328

Attal, M., Lavé, J., 2006. Changes of bedload characteristics along the Marsyandi River (central Nepal): Implications for understanding hillslope sediment supply, sediment load evolution along fluvial networks, and denudation in active orogenic belts. Tectonics, Clim. Landsc. Evol. 398, 143–171. doi:10.1130/2006.2398(09).

Attal, M., Mudd, S.M., Hurst, M.D., Weinman, B., Yoo, K., Naylor, M., 2015. Impact of change in erosion rate and landscape steepness on hillslope and fluvial sediments grain size in the Feather River basin (Sierra Nevada, California). Earth Surf. Dyn. 3, 201–222. doi:10.5194/esurf-3-201-2015

Balco, G., Stone, J.O., Lifton, N.A., Dunai, T.J., 2008. A complete and easily accessible means of calculating surface exposure ages or erosion rates from 10Be and 26Al measurements. Quat. Geochronol. 3, 174–195.

Balco, G., Stone, J.O.H., 2005. Measuring middle Pleistocene erosion rates with cosmic-ray-produced nuclides in buried alluvial sediment, Fisher Valley, southeastern Utah. Earth Surf. Process. Landforms 30, 1051–1067.

doi:10.1002/esp.1262

Belmont, P., Pazzaglia, F.J., Gosse, J.C., 2007. Cosmogenic 10Be as a tracer for hillslope and channel sediment dynamics in the Clearwater River, western Washington State. Earth Planet. Sci. Lett. 264, 123–135. doi:10.1016/j.epsl.2007.09.013

Bennett, G.L., Miller, S.R., Roering, J.J., Schmidt, D.A., 2016. Landslides, threshold slopes, and the survival of relict terrain in the wake of the Mendocino Triple Junction. Geology 44, 363–366. doi:10.1130/G37530.1

Bierman, P., Steig, E.J., 1996. Estimating rates of denudation using cosmogenic isotope abundances in sediment. Earth Surf. Process. Landforms 21, 125–139. doi:10.1002/(SICI)1096-9837(199602)21:2<125::AID-ESP511>3.0.CO;2-8

Binnie, S.A., Phillips, W.M., Summerfield, M.A., Fifield, L.K., 2007. Tectonic uplift, threshold hillslopes, and denudation rates in a developing mountain range. Geology 35, 743–746. doi:10.1130/G23641A.1

Bookhagen, B., Strecker, M.R., 2012. Spatiotemporal trends in erosion rates across a pronounced rainfall gradient: Examples from the southern Central Andes. Earth Planet. Sci. Lett. 327, 97–110. doi:10.1016/j.epsl.2012.02.005

Borchers, B., Marrero, S., Balco, G., Caffee, M., Goehring, B., Lifton, N., Nishiizumi, K., Phillips, F., Schaefer, J., Stone, J., 2016. Geological calibration of spallation production rates in the CRONUS-Earth project. Quat. Geochronol. 31, 188–198. doi:10.1016/j.quageo.2015.01.009

Brown, E.T., Stallard, R.F., Larsen, M.C., Raisbeck, G.M., Yiou, F., 1995. Denudation rates determined from the accumulation of in situ-produced Be10 in the Luquillo Experimental Forest, Puerto Rico. Earth Planet. Sci. Lett. 129, 193–202. doi:10.1016/0012-821X(94)00249-X

Burbank, D.W., Leland, J., Fielding, E., Anderson, R.S., Brozovic, N., Reid, M.R., Duncan, C., 1996. Bedrock incision, rock uplift and threshold hillslopes in the northwestern Himalayas. Nature 379, 505–510.

Carretier, S., Regard, V., Vassallo, R., Aguilar, G., Martinod, J., Riquelme, R., Christophoul, F., Charrier, R., Gayer, E., Farías, M., Audin, L., Lagane, C., 2015. Differences in 10Be concentrations between river sand, gravel and pebbles along the western side of the central Andes. Quat. Geochronol. 27, 33–51. doi:10.1016/j.quageo.2014.12.002

Carretier, S., Regard, V., Vassallo, R., Aguilar, G., Martinod, J., Riquelme, R., Pepin, E., Charrier, R., Hérail, G., Farías, M., Guyot, J.L., Vargas, G., Lagane, C., 2013. Slope and climate variability control of erosion in the Andes of central Chile. Geology 41, 195–198. doi:10.1130/G33735.1

Chmeleff, J., von Blanckenburg, F., Kossert, K., Jakob, D., 2010. Determination of the 10Be half-life by multicollector ICP-MS and liquid scintillation counting. Nucl. Instruments Methods Phys. Res. Sect. B Beam Interact. with Mater. Atoms 268, 192–199. doi:10.1016/j.nimb.2009.09.012

Codilean, A.T., Fenton, C.R., Fabel, D., Bishop, P., Xu, S., 2014. Discordance between cosmogenic nuclide concentrations in amalgamated sands and individual fluvial pebbles in an arid zone catchment. Quat. Geochronol. 19, 173–180.

doi:10.1016/j.quageo.2012.04.007

DiBiase, R.A., Whipple, K.X., Heimsath, A.M., Ouimet, W.B., 2010. Landscape form and millennial erosion rates in the San Gabriel Mountains, CA. Earth Planet. Sci. Lett. 289, 134–144. doi:10.1016/j.epsl.2009.10.036

García, V.H., Hongn, F., Cristallini, E.O., 2013. Late Miocene to recent morphotectonic evolution and potential seismic hazard of the northern Lerma valley: Clues from Lomas de Medeiros, Cordillera Oriental, NW Argentina. Tectonophysics 608, 1238–1253. doi:10.1016/j.tecto.2013.06.021

Garcin, Y., Schildgen, T.F., Torres Acosta, V., Melnick, D., Guillemoteau, J., Willenbring, J., Strecker, M.R., 2017. Short-lived increase in erosion during the African Humid Period: Evidence from the northern Kenya Rift. Earth Planet. Sci. Lett. 459, 58–69. doi:10.1016/j.epsl.2016.11.017

Granger, D.E., Kirchner, J.W., Finkel, R., 1996. Spatially averaged long-term erosion rates measured from in situ-produced cosmogenic nuclides in alluvial sediment. J. Geol. 104, 249–257.

Hain, M.P., Strecker, M.R., Bookhagen, B., Alonso, R.N., Pingel, H., Schmitt, a. K., 2011. Neogene to Quaternary broken foreland formation and sedimentation dynamics in the Andes of NW Argentina (25°S). Tectonics 30.2. doi:10.1029/2010TC002703

Hilley, G.E., Strecker, M.R., 2005. Processes of oscillatory basin filling and excavation in a tectonically active orogen: Quebrada del Toro Basin, NW Argentina. Bull. Geol. Soc. Am. 117, 887–901. doi:10.1130/B25602.1

Kober, F., Hippe, K., Salcher, B., Ivy-Ochs, S., Kubik, P.W., Wacker, L., Hählen, N., 2012. Debris-flow-dependent variation of cosmogenically derived catchment-wide denudation rates. Geology 40, 935–938. doi:10.1130/G33406.1

Korschinek, G., Bergmaier, A., Faestermann, T., Gerstmann, U.C., Knie, K., Rugel, G., Wallner, A., Dillmann, I., Dollinger, G., von Gostomski, C.L., Kossert, K., Maiti, M., Poutivtsev, M., Remmert, A., 2010. A new value for the half-life of 10Be by heavy-ion elastic recoil detection and liquid scintillation counting. Nucl. Instruments Methods Phys. Res. Sect. B Beam Interact. with Mater. Atoms 268, 187–191. doi:10.1016/j.nimb.2009.09.020

Lal, D., 1991. Cosmic ray labeling of erosion surfaces: in situ nuclide production rates and erosion models. Earth Planet. Sci. Lett. 104, 424–439. doi:10.1016/0012-821X(91)90220-C

Larsen, I.J., Montgomery, D.R., 2012. Landslide erosion coupled to tectonics and river incision. Nat. Geosci. 5, 468–473. doi:10.1038/ngeo1479

Lupker, M., Lavé, J., France-lanord, C., Christl, M., Bourlès, D., 2017. 10Be systematics in the Tsangpo-Brahmaputra catchment: the cosmogenic nuclide legacy of the eastern Himalayan syntaxis. Earth Surf. Dyn. doi:10.5194/esurf-5-429-2017

Marrett, R., Strecker, M.R., 2000. Response of intracontinental deformation in the central Andes to late Cenozoic reorganization of South American Plate motions. Tectonics 19, 452–467.

Marshall, J.A., Sklar, L.S., 2012. Mining soil databases for landscape-scale patterns in the abundance and size distribution of hillslope rock fragments. Earth Surf.

Process. Landforms 37, 287–300. doi:10.1002/esp.2241

Matmon, A., Bierman, P.R., Larsen, J., Southworth, S., Pavich, M., Finkel, R., Caffee, M., 2003. Erosion of an ancient mountain range, the Great Smoky Mountains, North Carolina and Tennessee. Am. J. Sci. 303, 817–855.

Mikuz, T., 2003. Tectonic and climatic controls on mountain-front collapse in Sierra Pasha, Cordillera Oriental; Salta Province; northwest Argentina. unpubl. Diploma thesis, Univ. Vienna 87–97.

Niemi, N. a., Oskin, M., Burbank, D.W., Heimsath, A.M., Gabet, E.J., 2005. Effects of bedrock landslides on cosmogenically determined erosion rates. Earth Planet. Sci. Lett. 237, 480–498. doi:10.1016/j.epsl.2005.07.009

Omarini, R.H., Sureda, R.J., Götze, H.-J., Seilacher, A., Pflüger, F., 1999. Puncoviscana folded belt in northwestern Argentina: testimony of Late Proterozoic Rodinia fragmentation and pre-Gondwana collisional episodes. Int. J. Earth Sci. 88, 76–97.

Ouimet, W.B., Whipple, K.X., Granger, D.E., 2009. Beyond threshold hillslopes: Channel adjustment to base-level fall in tectonically active mountain ranges. Geology 37, 579–582. doi:10.1130/G30013A.1

Paasche, Ø., Strømsøe, J.R., Dahl, S.O., Linge, H., 2006. Weathering characteristics of arctic islands in northern Norway. Geomorphology 82, 430–452. doi:10.1016/j.geomorph.2006.05.016

Palumbo, L., Hetzel, R., Tao, M., Li, X., 2009. Topographic and lithologic control on catchment-wide denudation rates derived from cosmogenic 10Be in two mountain ranges at the margin of NE Tibet. Geomorphology 117, 130–142. doi:10.1016/j.geomorph.2009.11.019

Puchol, N., Lavé, J., Lupker, M., Blard, P., Gallo, F., France-Lanord, C., Team, A., 2014. Grain-size dependent concentration of cosmogenic 10Be and erosion dynamics in a landslide-dominated Himalayan watershed. Geomorphology 224, 55–68. doi:10.1016/j.geomorph.2014.06.019

Reyes, F.C., Salfity, J.A., 1973. Stratigraphy considerations about the Cretaceous (Pirgua Subgroup) in Northwestern Argentina. Quinto Congr. Geológico Argentino 3.

Riebe, C.S., Granger, D.E., 2013. Quantifying effects of deep and near-surface chemical erosion on cosmogenic nuclides in soils, saprolite, and sediment. Earth Surf. Process. Landforms 38, 523–533. doi:10.1002/esp.3339

Riebe, C.S., Sklar, L.S., Lukens, C.E., Shuster, D.L., 2015. Climate and topography control the size and flux of sediment produced on steep mountain slopes. Proc. Natl. Acad. Sci. 112, 15574–15579. doi:10.1073/pnas.1503567112

Roda-Boluda, D.C., D’Arcy, M., McDonald, J., Whittaker, A.C., 2018. Lithological controls on hillslope sediment supply: insights from landslide activity and grain size distributions. Earth Surf. Process. Landforms. doi:10.1002/esp.4281

Ruxton, B.P., Beery, L., 1957. Weathering of granite and associated erosional features in Hong Kong. Geol. Soc. Am. Bull. 68, 1263–1292.

Schaller, M., von Blanckenburg, F., Hovius, N., Veldkamp, A., van den Berg, M.W., Kubik, P.W., 2004. Paleoerosion rates from cosmogenic 10Be in a 1.3 Ma terrace sequence: Response of the River Meuse to changes in climate and rock uplift. J. Geol. 112, 127–144.

Schaller, M., Von Blanckenburg, F., Veldkamp, A., Tebbens, L.A., Hovius, N., Kubik, P.W., 2002. A 30 000 yr record of erosion rates from cosmogenic 10Be in Middle European river terraces. Earth Planet. Sci. Lett. 204, 307–320. doi:10.1016/S0012-821X(02)00951-2

Scherler, D., Bookhagen, B., Strecker, M.R., 2014. Tectonic control on 10Be-derived erosion rates in the Garhwal Himalaya, India. J. Geophys. Res. Earth Surf. 119, 83–105. doi:10.1002/2013JF002955

Schildgen, T.F., Robinson, R.A.J., Savi, S., Phillips, W.M., Spencer, J.Q.G., Bookhagen, B., Scherler, D., Tofelde, S., Alonso, R.N., Kubik, P.W., Binnie, S.A., Strecker, M.R., 2016. Landscape response to late Pleistocene climate change in NW Argentina: Sediment flux modulated by basin geometry and connectivity. J. Geophys. Res. Earth Surf. 121, 392–414. doi:10.1002/2015JF003607

Schwab, K., Schäfer, A., 1976. Sedimentation und Tektonik im mittleren Abschnitt des Rio Toro in der 0stkordillere NW-Argentiniens. Geol. Rundschau 65, 175–194. doi:10.1007/BF01808462

Schwanghart, W., Scherler, D., 2014. TopoToolbox 2 – MATLAB-based software for topographic analysis and modeling in Earth surface sciences. Earth Surf. Dyn. 2, 1–7. doi:10.5194/esurf-2-1-2014

Sklar, L.S., Riebe, C.S., Marshall, J.A., Genetti, J., Leclere, S., Lukens, C.L., Merces, V., 2017. The problem of predicting the size distribution of sediment supplied by hillslopes to rivers. Geomorphology 277, 31–49. doi:10.1016/j.geomorph.2016.05.005

Stone, J.O., 2000. Air pressure and cosmogenic isotope production. J. Geophys. Res. Solid Earth 105, 23753–23759. doi:10.1029/2000JB900181

Tofelde, S., Schildgen, T.F., Savi, S., Pingel, H., Wickert, A.D., Bookhagen, B., Wittmann, H., Alonso, R.N., Cottle, J., Strecker, M.R., 2017. 100 kyr fluvial cut-and-fill terrace cycles since the Middle Pleistocene in the southern Central Andes, NW Argentina. Earth Planet. Sci. Lett. 473, 141–153. doi:10.1016/j.epsl.2017.06.001

Trauth, M.H., Strecker, M.R., 1999. Formation of landslide-dammed lakes during a wet period between 40,000 and 25,000 yr B.P. in northwestern Argentina. Palaeogeogr. Palaeoclimatol. Palaeoecol. 153, 277–287.

von Blanckenburg, F., Hewawasam, T., Kubik, P.W., 2004. Cosmogenic nuclide evidence for low weathering and denudation in the wet, tropical highlands of Sri Lanka. J. Geophys. Res. Earth Surf. 109. doi:10.1029/2003JF000049

West, A.J., Hetzel, R., Li, G., Jin, Z., Zhang, F., Hilton, R.G., Densmore, A.L., 2014. Dilution of 10Be in detrital quartz by earthquake-induced landslides: Implications for determining denudation rates and potential to provide insights into landslide sediment dynamics. Earth Planet. Sci. Lett. 396, 143–153. doi:10.1016/j.epsl.2014.03.058

Whittaker, A.C., Attal, M., Allen, P.A., 2010. Characterising the origin, nature and fate of sediment exported from catchments perturbed by active tectonics. Basin Resea 22, 809–828. doi:10.1111/j.1365-2117.2009.00447.x

Wittmann, H., von Blanckenburg, F., Kruesmann, T., Norton, K.P., Kubik, P.W., 2007. Relation between rock uplift and denudation from cosmogenic nuclides in river sediment in the Central Alps of Switzerland. J. Geophys. Res. 112, F04010. doi:10.1029/2006JF000729

Wobus, C., Whipple, K.X., Kirby, E., Snyder, N., Johnson, J., Spyropolou, K., Crosby, B., Sheehan, D., 2006. Tectonics from topography: procedurses, promise, and pitfalls. Geol. Soc. Am. Spec. Pap. 398, 55–74. doi:10.1130/2006.2398(04).

Yanites, B.J., Tucker, G.E., Anderson, R.S., 2009. Numerical and analytical models of cosmogenic radionuclide dynamics in landslide-dominated drainage basins. J. Geophys. Res. Earth Surf. 114. doi:10.1029/2008JF001088

Supplementary material

Effects of deep-seated versus shallow hillslope processes on cosmogenic ^{10}Be concentrations in fluvial sand and gravel

Stefanie Tofelde[*1,2], Walter Duesing[2], Taylor F. Schildgen[1,2], Andrew D. Wickert[3], Hella Wittmann[1], Ricardo N. Alonso[4,] Manfred Strecker[2]

[1]*Helmholtz Zentrum Potsdam, GeoForschungsZentrum (GFZ) Potsdam, 14473 Potsdam, Germany.*
[2]*Institut für Erd- und Umweltwissenschaften, Universität Potsdam, 14476 Potsdam, Germany.*
[3]*Department of Earth Sciences and Saint Anthony Falls Laboratory, University of Minnesota, Minneapolis, MN 55455, USA.*
[4]*Departamento de Geología, Universidad Nacional de Salta, 4400 Salta, Argentina.*

1. Hillslope-process inventory

To create the erosion-process inventory, we mapped the four main types of hillslope erosion processes within our study area. The four types include 1) *low-slope gullying*, 2) *scree production*, 3) *steep-slope gullying*, and 4) *deep-seated landsliding*. The areas affected by any of those processes were mapped as a shapefile in Google Earth and later imported in ArcGIS. The total area for each process was calculated (**Table S1**). However, to calculate the areas covered by any of those polygons, the total polygon area is reduced, because the 3D view in which the mapping took place is simplified to a 2D map view. Consequently, steep polygons are reduced more in surface area than are gently-sloping polygons. Therefore, the *steep-slope gully erosion* and *deep-seated landslides*, which often occur on the steeper slopes, are probably underestimated in size compared to *low-slope gullying*, which dominantly occurs on more gentle slopes. However, if we were able to correct for this effect, it would only make our observations of a change in processes with increasing slopes and erosion rates more pronounced.

We most likely overestimate the area covered by diffusion, which we define as the remaining area that is not affected by any of the four previously mentioned processes. The remaining area, however, also includes the river channel system itself, for which we do not correct. Because we focus our analysis on the few percent area covered by those four processes, and not on the diffusive part, a slight decrease in those numbers would not affect our results.

Table S1 *Surface area affected by each of the mapped hillslope processes in absolute and relative values.*

Sample site	Land-slide (m2)	Steep-slope gully (m2)	Scree (m2)	Low-slope gully (m2)	Diffusion (m2)	Total (m2)	Land-slide (%)	Steep-slope gully (%)	Scree (%)	Low-slope gully (%)	Diffu-sion (%)
M08	0	1787137	4695915	26044859	2156452732	2188980643	0.00	0.08	0.21	1.19	98.51
T11	0	26670	612651	23733376	105212358	129585054	0.00	0.02	0.47	18.31	81.19
M15	0	1512998	3355033	19496086	1636942340	1661306457	0.00	0.09	0.20	1.17	98.53
M48	47596	12006126	11601206	101322570	2826979557	2951957055	0.00	0.41	0.39	3.43	95.77
M60	0	1512998	2591408	6826561	1477472738	1488403705	0.00	0.10	0.17	0.46	99.27
T68	0	108809	1231931	2283230	469877317	473501287	0.00	0.02	0.26	0.48	99.23
T69	0	589313	1021581	466598	74892137	76969629	0.00	0.77	1.33	0.61	97.30
T26	11337	614388	0	0	32344068	32969793	0.03	1.86	0.00	0.00	98.10
T27	42972	127004	0	0	9312056	9482033	0.45	1.34	0.00	0.00	98.21
T28	0	2138976	1750263	1385814	108041227	113316281	0.00	1.89	1.54	1.22	95.34
T32	25271	262907	42505	0	10124189	10454872	0.24	2.51	0.41	0.00	96.84
T35	0	250865	585928	747772	99183860	100768425	0.00	0.25	0.58	0.74	98.43
T43	4876	9123614	2589246	8417986	747404261	767539983	0.00	1.19	0.34	1.10	97.38
T44	22689	5345148	1285179	245287	167740806	174639109	0.01	3.06	0.74	0.14	96.05
T59	0	572447	434474	940392	96464304	98411617	0.00	0.58	0.44	0.96	98.02
C1*	0	1512998	3355033	19711302	1639521600	1664100933	0.00	0.09	0.20	1.18	98.52
C2*	0	108811	1341989	3646528	488132815	493230143	0.00	0.02	0.27	0.74	98.97
C3*	0	26670	612651	23743239	105502291	129884851	0.00	0.02	0.47	18.28	81.23
C5*	4604	1876183	621441	4290367	170108080	176900674	0.00	1.06	0.35	2.43	96.16
C6*	100160	17863470	4026998	9993932	975915978	1007900538	0.01	1.77	0.40	0.99	96.83

2. Remote sensing analysis

Topographic and climatic data for all catchments are summarized in **Table S2**. The correlation between the different parameters and sand-derived basin mean denudation rates are shown in **Figure S1**.

2.1. Slope

Our slope analysis is based on the ~30 m resolution SRTM digital elevation model (DEM) (data available from the U.S. Geological Survey). The slope is calculated for each pixel as the maximum rate of change in elevation between that pixel cell and its neighbouring 8 cells. Then, a median slope value for the entire catchment is calculated. Previous studies have shown, that the standard deviation of the slope value depends on the resolution of the DEM (Ouimet et al., 2009), making it less meaningful. We therefore report no standard deviation, but only the mean and median values (**Table S2**) and the slope distributions (**Fig. 5**).

2.2. Channel steepness index

From the SRTM DEM, we extract the longitudinal river profiles for each catchment. Typical river profiles have a concave up shape, and empirical data have shown a power-law relationship between channel slope (S) and drainage area (A), known as Flint's law:

$$S = k_s A^{-\theta} \tag{2}$$

where k_s is the steepness index and θ the concavity (Kirby and Whipple, 2001). However, to be able to compare several catchment areas, Wobus et al. (2006) suggested to calculate a normalized steepness index, k_{sn}, by using a reference concavity value, θ_{ref}. The reference concavity used is typically 0.45.

To calculate the k_{sn} values for the drainage system in the Quebrada del Toro, we used tools within Topotoolbox (Schwanghart and Kuhn, 2010). k_{sn} values were calculated for streams with a minimum drainage area of 1 km^2 and values were averaged over stream segments of 1 km. Finally, we calculated the average k_{sn} value of all stream segments within each catchment. Ouimet et al., 2009 suggested to use k_{sn} as a metric for erosion rate instead of mean basin slope, because plots of erosion rate versus mean slope reach a saturation when the hillslopes reach threshold slopes. However, in the Quebrada del Toro, the k_{sn} values also seem to reach a saturation value (**Figure S1B**). Similar behavior can be observed in the Apennines, Italy (Cyr et al., 2010) and the San Gabriel Mountains, USA (DiBiase et al., 2010), where k_{sn} values never exceed 200. We thus prefer to compare our erosion rates with mean hillslope angles, considering that we later investigate erosion processes on those hillslopes.

2.3. Relief

Basin relief is defined as the difference between maximum and minimum elevation within a defined radius. Because some of our catchment areas are as small as 9 km^2, we calculated basin relief using focal statistics in ArcGIS with a 2-km radius around each pixel (equivalent to 68 cells in our ~30 m resolution DEM). Then we calculated the basin mean value.

2.4. Rainfall

Mean annual rainfall (MAR) was calculated from the TRMM2B31 product with a 5 km resolution, calibrated for our study region by Bookhagen and Strecker (2008). The TRMM product only includes rainfall, and does not include snowfall. However, in our study region, there are virtually no glaciated peaks. As such, the contribution from snow-and icemelt to streamflow is negligible, instead the vast majority of precipitation falls as rain. The basin mean denudation rates show no clear trend with mean annual rainfall (**Figure S1D**), contrary to previous findings in NW Argentina (Bookhagen and Strecker, 2012). However, Bookhagen and Strecker (2012) investigated a large region with a pronounced gradient in rainfall, whereas the rainfall gradient in the Quebrada del Toro (MAR = 130 to 626 mm/yr) may not be strong enough to dominate the denudation signal.

2.5. Vegetation cover

We determined the relative difference in vegetation cover between the catchment using the Enhanced Vegetation Index (EVI). EVI is calculated using the following equation (Huete et al., 2002):

$$\mathrm{EVI} = G * \frac{(\mathrm{NIR}-\mathrm{RED})}{(\mathrm{NIR}+C1*\mathrm{RED}-C2*\mathrm{BLUE}+L)} \qquad (3)$$

We used a pre-processed EVI map, calculated from the MODIS product MOD13A1, which has a 500 m resolution and a 16 day compositing period (Didan, 2009). However, because we are not interested in temporal but rather spatial changes in vegetation cover, we used a single product recorded in January 2014 that represents summer vegetation. Although no clear trend is obvious, in general, we observe higher EVI values (indicating denser vegetation) in regions with higher denudation rates (**Figure S1E**). This is different from previous observation, for instance in East Africa, where Acosta et al. (2015) observed significant differences in denudation rates for the same slopes between densely and sparsely vegetated areas. One important difference compared to East Africa is that in the Quebrada del Toro, the densely vegetated parts are exclusively found close to the basin outlet and coincide with the steepest slopes. Thus, the slopes might be too steep for vegetation cover to have a protective and erosion-reducing effect.

__Table S__ 2 Topographic and climatic characteristics of the catchments.

Sample site	Mean elevation (m)	Median elevation (m)	Mean basin slope (°)	Median basin slope (°)	Mean ksn	Median ksn	Mean relief 2 km (m)	Median relief 2 km (m)	Mean annual rainfall (mm)	Median annual rainfall (mm)	Mean EVI	Median EVI	D_{50} (mm)	*NSGI*
M08	3801	3724	15.9	15.6	83	66	668	637	189	179	0.08	0.08	25	-0.04
T11	3497	3395	13.5	11.6	93	86	645	568	161	124	0.06	0.06	31	-0.18
M15	3825	3736	15.5	14.9	78	60	654	625	188	176	0.08	0.08	19	-0.14
T26	2712	2630	30.8	32.2	174	170	1309	1291	584	534	0.44	0.47	50	0.77
T27	2433	2427	27.9	28.9	132	130	1021	1042	628	624	0.42	0.42	31	0.77
T28	3642	3748	24.5	25.4	121	116	914	943	141	121	0.07	0.07	20	-0.03
T32	3096	3064	29.1	30.0	172	196	1286	1322	130	90	0.20	0.21	28.5	0.49
T35	4128	3932	17.6	16.8	136	129	867	891	217	178	0.08	0.08	25	-0.22
T43	3741	3648	23.5	23.9	155	147	990	977	216	206	0.09	0.09		0.65
T44	3674	3657	26.8	28.2	191	188	1258	1236	191	184	0.17	0.17		0.79
M48	3701	3668	17.1	16.7	97	76	723	676	185	176	0.08	0.08	33	
T59	3615	3571	14.9	14.4	59	42	610	615	195	180	0.09	0.09	20.5	0.48
M60	3876	3771	15.7	15.2	75	59	665	638	190	176	0.09	0.08		
T68	3788	3719	17.6	17.9	98	85	719	673	186	185	0.09	0.09	30.5	0.18
T69	3745	3777	23.6	23.8	126	116	883	906	155	135	0.08	0.08	26	0.02
C1*	3824	3735	15.5	14.9	78	60	653	625	188	176	0.08	0.08	19	
C2*	3764	3705	17.5	17.7	99	86	715	673	189	185	0.09	0.08	30.5	
C3*	3495	3393	13.5	11.5	93	86	645	567	161	124	0.06	0.06	31	
C5*	3703	3591	19.3	18.8	149	135	872	866	163	83	0.09	0.08	27.5	
C6*	3666	3588	24.5	25.1	165	154	1055	1043	215	206	0.11	0.09	26	

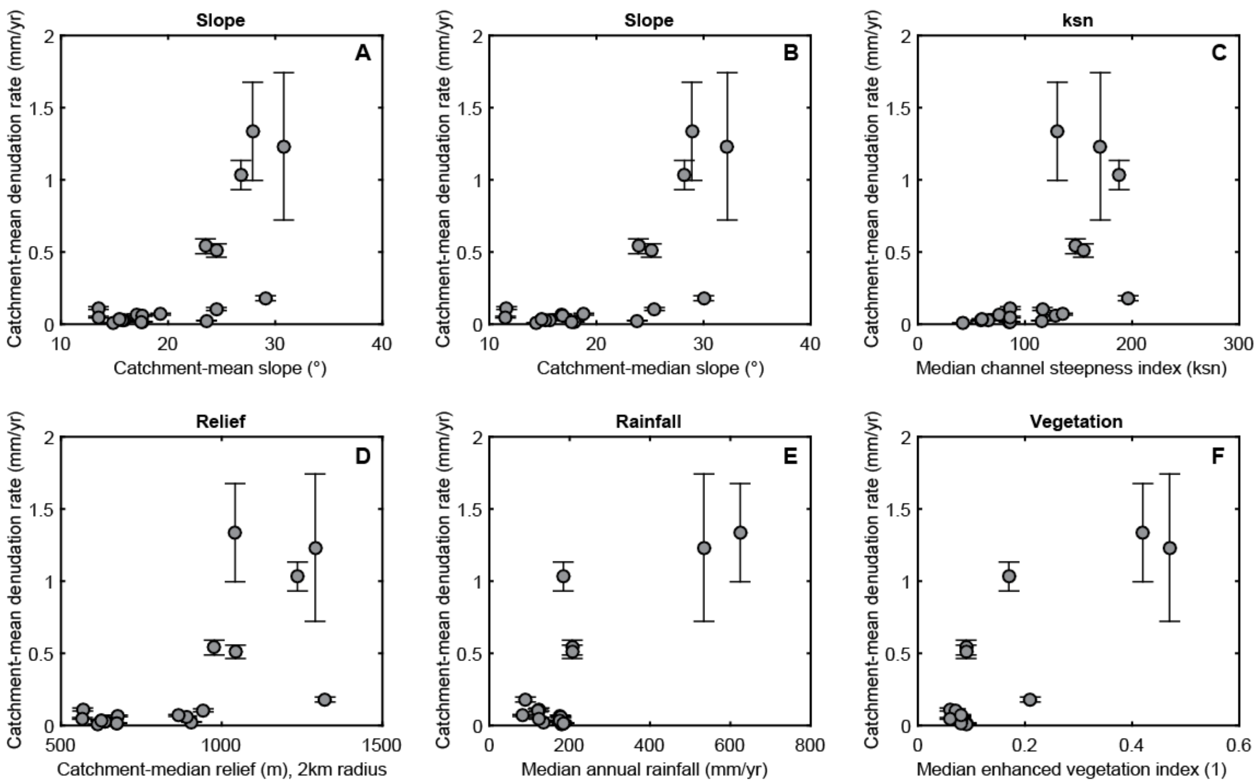

***Figure S1** Basin mean denudation rates compared to topographic (A,B,C,D) and climatic (E,F) parameters.*

3. Previous studies of ^{10}Be in different grain sizes

Table S 3 *Detailed list of cosmogenic nuclide studies that have measured* ^{10}Be *concentrations in a sand and a gravel fraction for the same location. The list is an update of the compilation by* Codilean et al., (2014)*, which was itself updated by* Carretier et al., (2015)*.*

Reference	**Title**	**Grain sizes (mm) sand and pebbles**
(Aguilar et al., 2014)	Grain size-dependent ^{10}Be concentrations in alluvial stream sediment of the Huasco Valley, a semi-arid Andes region	0.5 – 1 10 – 30 50 - 100
(Belmont et al., 2007)	Cosmogenic ^{10}Be as a tracer for hillslope and channel sediment dynamics in the Clearwater River, western Washington State	0.25 – 0.5 22.6 - 90
(Brown et al., 1995)	Denudation rates determined from the accumulation of in situ-produced ^{10}Be in the Luquillo experimental forest, Puerto Rico	0.25 – 0.5 gravel
(Carretier et al., 2015)	Differences in ^{10}Be concentrations between river sand, gravel and pebbles along the western side of the central Andes	0.5 – 1 10 - 30 50 - 100
(Clapp et al., 2002)	Using ^{10}Be and ^{26}Al to determine sediment generation rates and identify sediment source areas in an arid region drainage basin	0.25 – 0.5 0.5 – 1 – 2 – 4 4 – 12.7 > 12.7
(Codilean et al., 2014)	Discordance between cosmogenic nuclide concentrations in amalgamated sands and individual fluvial pebbles in an arid zone catchment	0.25 – 0.5 16-21
(Delunel et al., 2014)	Transient sediment supply in a high-altitude Alpine environment evidenced through a ^{10}Be budget of the Etages catchment (French Western Alps)	0.125 – 0.25 0.25 – 0.5 1 – 4 4 - 10 10 – 20 (1 sample) 50 - 100
(Heimsath et al., 2010)	Eroding Australia: rates and processes from Bega Valley to Arnhem Land	sand and gravel
(Hewawasam et al., 2003)	Increase of human over natural erosion rates in tropical highlands constrained by cosmogenic nuclides	0.25 – 0.5 1 – 2 2 – 3 3 – 6 12 - 20
(Matmon et al., 2003)	Erosion of an ancient mountain range, the Great Smoky Mountains, North Carolina and Tennessee	0.25 – 0.85 0.85 – 2 2 – 10 10 - 20
(Matmon et al., 2005)	Dating offset fans along the Mojave section of the San Andreas fault using	0.25 – 0.85 0.85 – 2 2 – 10 > 10

(Oskin et al., 2008)	Elevated shear zone loading rate during an earthquake cluster in eastern California	sand and pebble
(Reinhardt et al., 2007)	Interpreting erosion rates from cosmogenic radionuclide concentrations measured in rapidly eroding terrain	0.25 – 0.5 8 – 16
(Palumbo et al., 2009)	Topographic and lithologic control on catchment-wide denudation rates derived from cosmogenic ^{10}Be in two mountain ranges at the margin of NE Tibet	0.2 – 0.71 20 - 200
(Puchol et al., 2014)	Grain-size dependent concentration of cosmogenic ^{10}Be and erosion dynamics in a landslide-dominated Himalayan watershed	0.075 - 0.25 0.25 - 0.5 0.5 – 1 1 - 2 2 – 4.7 4.7 – 40
(Savi et al., 2016)	Climatic controls on debris-flow activity and sediment aggradation: The Del Medio fan, NW Argentina	0.25 – 0.71 10 – 40
(Schildgen et al., 2016)	Landscape response to late Pleistocene climate change in NW Argentina: Sediment flux modulated by basin geometry and connectivity	0.25 – 0.71 10 – 30

4. Geological maps

Figure S2 shows the geological maps for each catchment (main stem and tributary) for which we collected cosmogenic radionuclide samples.

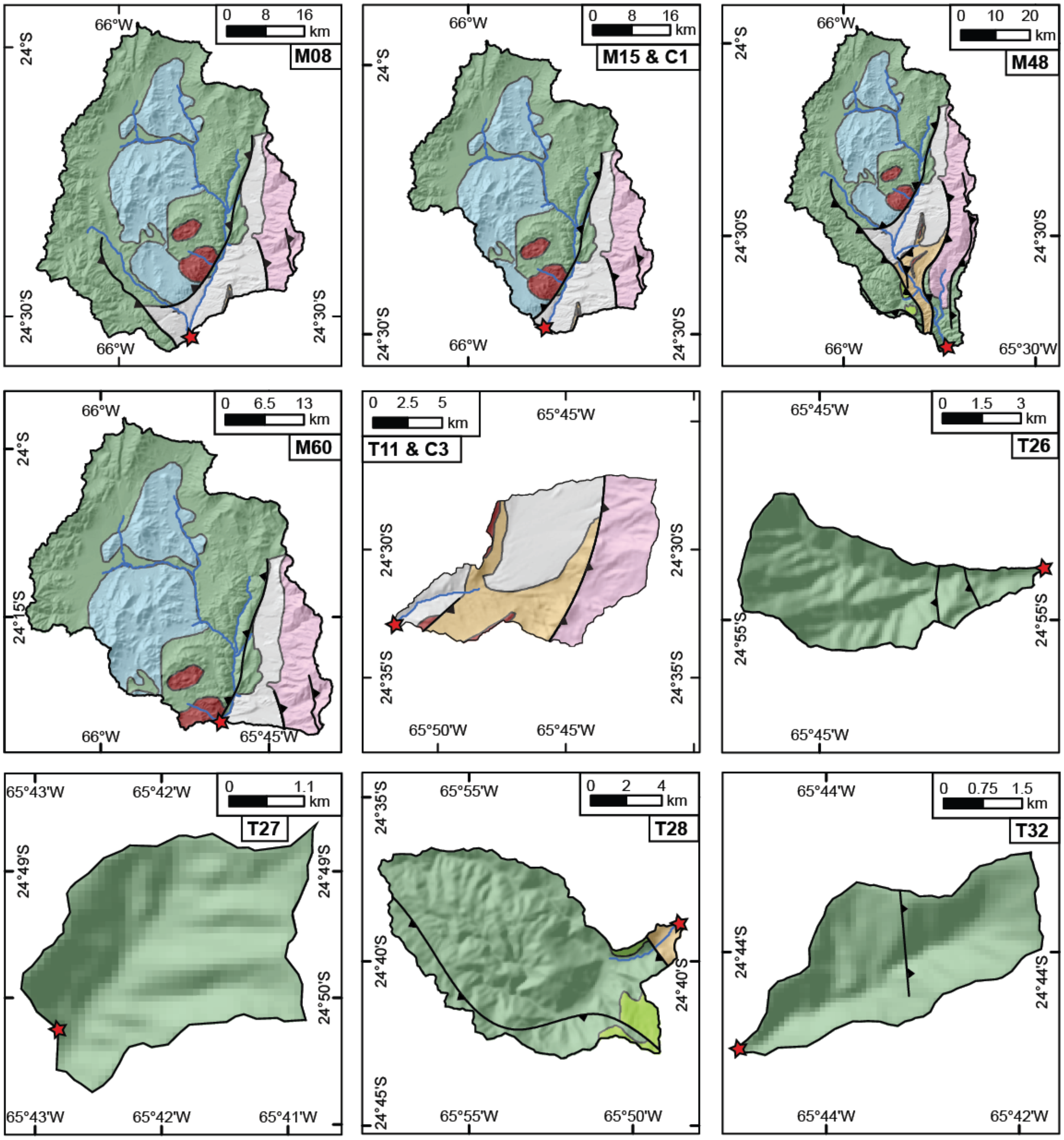

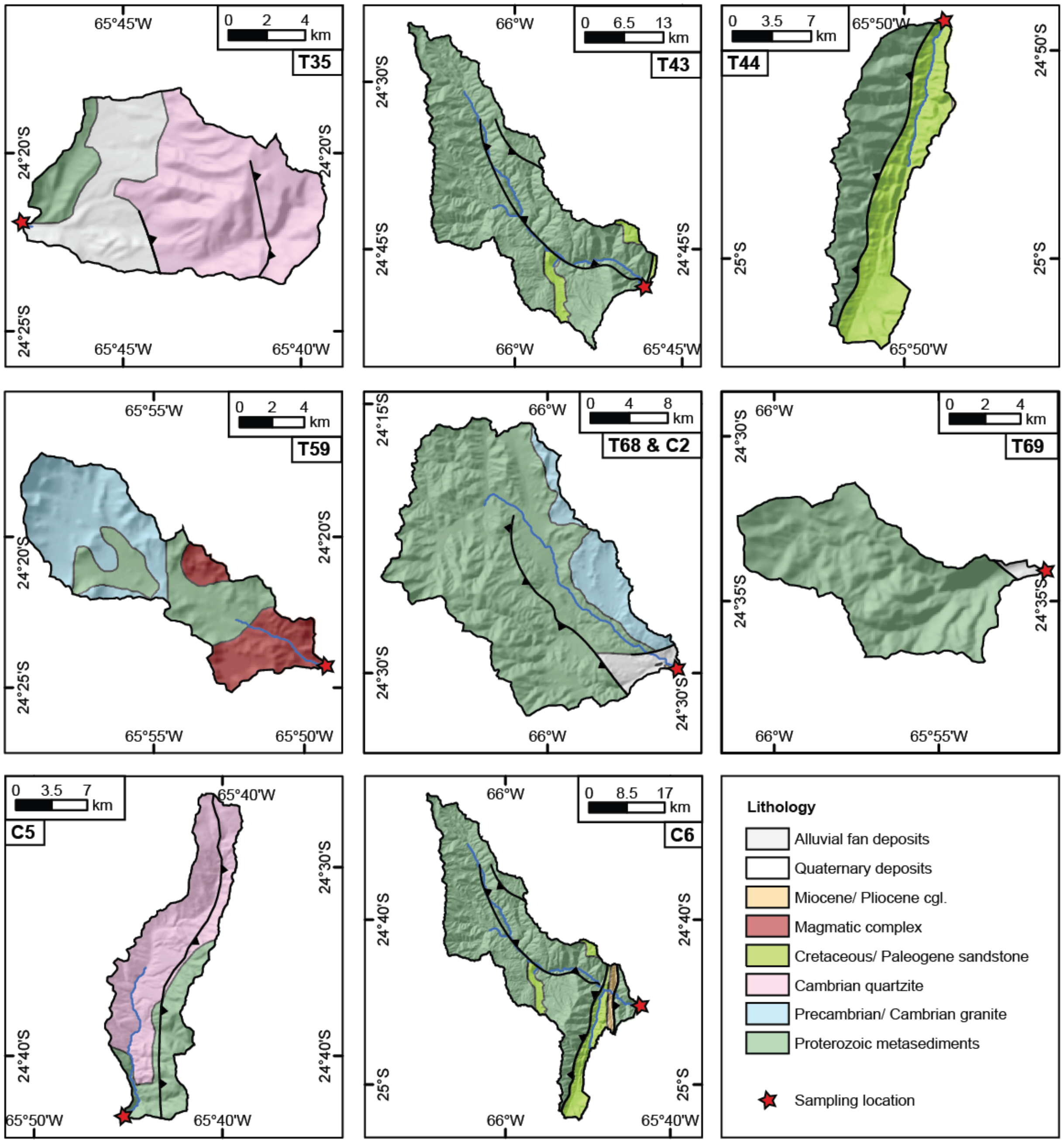

Figure S 2 Geological maps of all sampled catchments.

5. ^{10}Be differences in sand and gravel

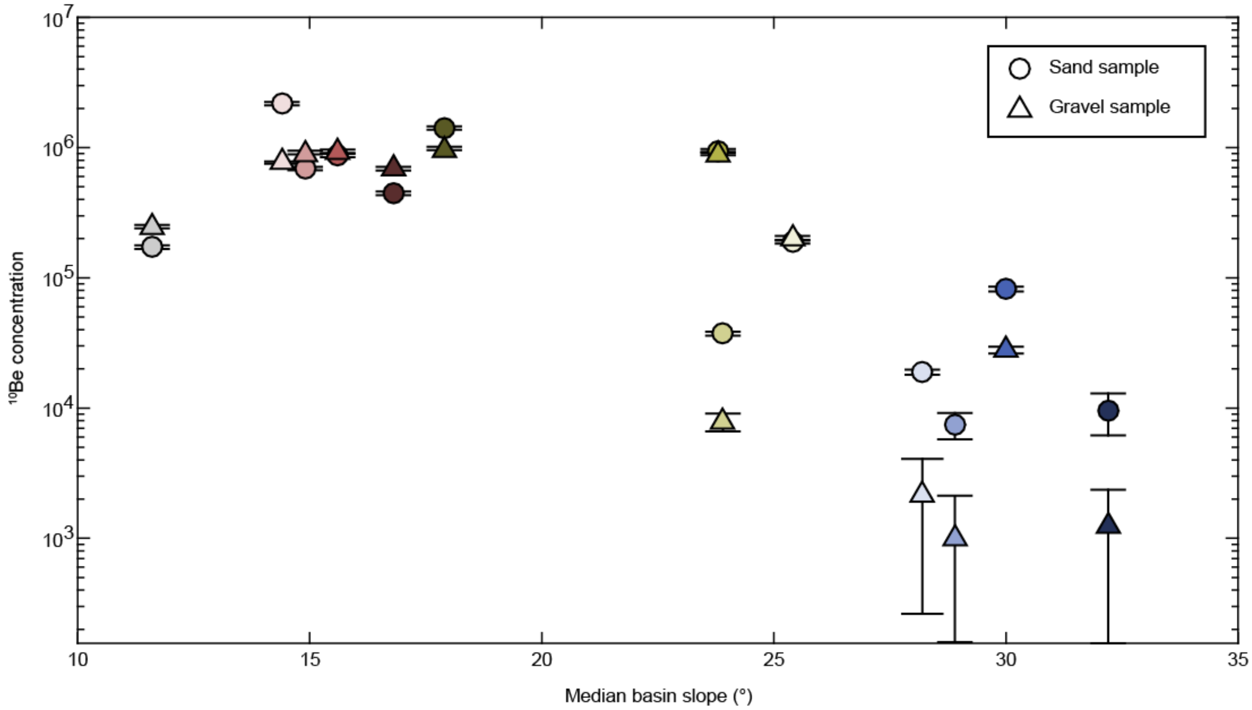

Figure S3 *^{10}Be concentration of the sand and gravel pairs compared to median basin slope. Each pair is represented by one color. Circles represent sand samples, triangles the gravel samples. Note that the y-axis is logarithmic. In steeper areas (> 25°) the ^{10}Be concentration in gravel is significantly lower than in the sand samples.*

References

Aguilar, G., Carretier, S., Regard, V., Vassallo, R., Riquelme, R., Martinod, J., 2014. Grain size-dependent 10Be concentrations in alluvial stream sediment of the Huasco Valley, a semi-arid Andes region. Quat. Geochronol. 19, 163–172. doi:10.1016/j.quageo.2013.01.011

Belmont, P., Pazzaglia, F.J., Gosse, J.C., 2007. Cosmogenic 10Be as a tracer for hillslope and channel sediment dynamics in the Clearwater River, western Washington State. Earth Planet. Sci. Lett. 264, 123–135. doi:10.1016/j.epsl.2007.09.013

Bookhagen, B., Strecker, M.R., 2012. Spatiotemporal trends in erosion rates across a pronounced rainfall gradient: Examples from the southern Central Andes. Earth Planet. Sci. Lett. 327, 97–110. doi:10.1016/j.epsl.2012.02.005

Bookhagen, B., Strecker, M.R., 2008. Orographic barriers, high-resolution TRMM rainfall, and relief variations along the eastern Andes. Geophys. Res. Lett. 35.6. doi:10.1029/2007GL032011

Brown, E.T., Stallard, R.F., Larsen, M.C., Raisbeck, G.M., Yiou, F., 1995. Denudation rates determined from the accumulation of in situ-produced Be10 in the Luquillo Experimental Forest, Puerto Rico. Earth Planet. Sci. Lett. 129, 193–202. doi:10.1016/0012-821X(94)00249-X

Carretier, S., Regard, V., Vassallo, R., Aguilar, G., Martinod, J., Riquelme, R., Christophoul, F., Charrier, R., Gayer, E., Farías, M., Audin, L., Lagane, C., 2015. Differences in 10Be concentrations between river sand, gravel and pebbles along the western side of the central Andes. Quat. Geochronol. 27, 33–51. doi:10.1016/j.quageo.2014.12.002

Clapp, E.M., Bierman, P.R., Caffee, M., 2002. Using 10Be and 26Al to determine sediment generation rates and identify sediment source areas in an arid region drainage basin. Geomorphology 45, 89–104.

Codilean, A.T., Fenton, C.R., Fabel, D., Bishop, P., Xu, S., 2014. Discordance between cosmogenic nuclide concentrations in amalgamated sands and individual fluvial pebbles in an arid zone catchment. Quat. Geochronol. 19, 173–180. doi:10.1016/j.quageo.2012.04.007

Cyr, a. J., Granger, D.E., Olivetti, V., Molin, P., 2010. Quantifying rock uplift rates using channel steepness and cosmogenic nuclide-determined erosion rates: Examples from northern and southern Italy. Lithosphere 2, 188–198. doi:10.1130/L96.1

Delunel, R., van der Beek, P.A., Bourlès, D.L., Carcaillet, J., Schlunegger, F., 2014. Transient sediment supply in a high-altitude Alpine environment evidenced through a 10Be budget of the Etages catchment (French Western Alps). Earth Surf. Process. Landforms 39, 890–899. doi:10.1002/esp.3494

DiBiase, R.A., Whipple, K.X., Heimsath, A.M., Ouimet, W.B., 2010. Landscape form and millennial erosion rates in the San Gabriel Mountains, CA. Earth Planet. Sci. Lett. 289, 134–144. doi:10.1016/j.epsl.2009.10.036

Didan, K., 2009. MOD13A1. 6. NASA EOSDIS Land Processes DAAC [WWW Document]. USGS Earth Resour. Obs. Sci. Center, Sioux Falls, South Dakota. doi:10.5067/MODIS/MOD13A1.006.

Heimsath, A.M., Chappell, J., Fifield, K., 2010. Eroding Australia: rates and processes from Bega Valley to Arnhem Land. Geol. Soc. London, Spec. Publ. 346, 225–241.

Hewawasam, T., von Blanckenburg, F., Schaller, M., Kubik, P., 2003. Increase of human over natural erosion rates in tropical highlands constrained by cosmogenic nuclides. Geology 31, 597–600.

Huete, A., Didan, K., Miura, T., Rodriguez, E.P., Gao, X., Ferreira, L.G., 2002. Overview of the radiometric and biophysical performance of the MODIS vegetation indices. Remote Sens. Environ. 83, 195–213.

Kirby, E., Whipple, K., 2001. Quantifying differential rock-uplift rates via stream profile analysis. Geology 29, 415–418. doi:10.1130/0091-7613(2001)029<0415:QDRURV>2.0.CO;2

Matmon, A., Bierman, P.R., Larsen, J., Southworth, S., Pavich, M., Finkel, R., Caffee, M., 2003. Erosion of an ancient mountain range, the Great Smoky Mountains, North Carolina and Tennessee. Am. J. Sci. 303, 817–855.

Matmon, A., Schwartz, D.P., Finkel, R., Clemmens, S., Hanks, T., 2005. Dating offset fans along the Mojave section of the San Andreas fault using cosmogenic 26Al and 10Be. GSA Bull. 117, 795–807. doi:10.1130/B25590.1

Oskin, M., Perg, L., Shelef, E., Strane, M., Gurney, E., Singer, B., Zhang, X., 2008. Elevated shear zone loading rate during an earthquake cluster in eastern California. Geology 36, 507–510. doi:10.1130/G24814A.1

Ouimet, W.B., Whipple, K.X., Granger, D.E., 2009. Beyond threshold hillslopes: Channel adjustment to base-level fall in tectonically active mountain ranges. Geology 37, 579–582. doi:10.1130/G30013A.1

Palumbo, L., Hetzel, R., Tao, M., Li, X., 2009. Topographic and lithologic control on catchment-wide denudation rates derived from cosmogenic 10Be in two mountain ranges at the margin of NE Tibet. Geomorphology 117, 130–142. doi:10.1016/j.geomorph.2009.11.019

Puchol, N., Lavé, J., Lupker, M., Blard, P., Gallo, F., France-Lanord, C., Team, A., 2014. Grain-size dependent concentration of cosmogenic 10Be and erosion dynamics in a landslide-dominated Himalayan watershed. Geomorphology 224, 55–68. doi:10.1016/j.geomorph.2014.06.019

Reinhardt, L.J., Hoey, T.B., Barrows, T.T., Dempster, T.J., Bishop, P., Fifield, L.K., 2007. Interpreting erosion rates from cosmogenic radionuclide concentrations measured in rapidly eroding terrain.

Earth Surf. Process. Landforms 32, 390–406. doi:10.1002/esp

Savi, S., Schildgen, T.F., Tofelde, S., Wittmann, H., Scherler, D., Mey, J., Alonso, R.N., Strecker, M.R., 2016. Climatic controls on debris-flow activity and sediment aggradation: The Del Medio fan, NW Argentina. J. Geophys. Res. Earth Surf. 2424–2445. doi:10.1002/2016JF003912

Schildgen, T.F., Robinson, R.A.J., Savi, S., Phillips, W.M., Spencer, J.Q.G., Bookhagen, B., Scherler, D., Tofelde, S., Alonso, R.N., Kubik, P.W., Binnie, S.A., Strecker, M.R., 2016. Landscape response to late Pleistocene climate change in NW Argentina: Sediment flux modulated by basin geometry and connectivity. J. Geophys. Res. Earth Surf. 121, 392–414. doi:10.1002/2015JF003607

Schwanghart, W., Kuhn, N.J., 2010. TopoToolbox: A set of Matlab functions for topographic analysis. Environ. Model. Softw. 25, 770–781. doi:10.1016/j.envsoft.2009.12.002

Torres Acosta, V., Schildgen, T.F., Clarke, B.A., Scherler, D., Bookhagen, B., Wittmann, H., von Blanckenburg, F., Strecker, M.R., 2015. Effect of vegetation cover on millennial-scale landscape denudation rates in East Africa. Lithosphere 7, 408–420. doi:10.1130/L402.1

Wobus, C., Whipple, K.X., Kirby, E., Snyder, N., Johnson, J., Spyropolou, K., Crosby, B., Sheehan, D., 2006. Tectonics from topography: procedurses, promise, and pitfalls. Geol. Soc. Am. Spec. Pap. 398, 55–74. doi:10.1130/2006.2398(04).